2011

A turbulence-based model for the primary breakup of pressure atomized liquid jets

Christopher D. Schmitz
Iowa State University

A turbulence-based model for the primary breakup of pressure atomized liquid jets

by

Christopher Schmitz

A thesis submitted to the graduate faculty

in partial fulfillment of the requirements for the degree of

MASTER OF SCIENCE

Major: Mechanical Engineering

Program of Study Committee:
Shankar Subramaniam, Major Professor
Terry Meyer
Gap-Yong Kim

Iowa State University

Ames, Iowa

2011

TABLE OF CONTENTS

LIST OF FIGURES

LIST OF TABLES

ABSTRACT

The primary objective of this study was to investigate and validate a predictive, turbulence based primary breakup model. The ESE model is based on a modeled evolution of the turbulent energy spectrum, and is sufficiently general that it may be applied to a broad range of pressure-atomized spray processes, such as those found in agricultural irrigation, industrial coating, automotive fuel injection, and others. In this study, the governing equations are derived and applied to diesel sprays to address a lack of predictive primary breakup models in literature. Tests are performed to demonstrate that the ESE model is numerically converged and has well-behaved model constants. Drop-size distributions are generated for the dense liquid region and compared with experimental and DNS results obtained from literature. Finally, it is proposed that the ESE model be coupled to an aerodynamically-based secondary breakup model to improve predictive capability under real 'diesel-like' conditions.

CHAPTER 1. INTRODUCTION

1.1 Motivation

The primary breakup process is most often characterized by the disintegration of an intact liquid core into initial droplets. It is the mechanism from which all subsequent spray processes originate. The need for better understanding and predictive models of primary atomization therefore spans across nearly every major industry today. Better understanding leads to increased profitability and decreased waste in industrial painting and coating applications. In agriculture, better atomization in irrigation systems leads to decreased water consumption and more precise application of pesticides. The impact fuel injector design has on diesel engine performance is paramount, governing such parameters as power output, combustion characteristics, fuel consumption, and pollution.

Despite its importance and numerous advances, the exact mechanism(s) responsible for primary breakup in high speed jets remains unresolved to this day. The need for better understanding of primary breakup is a very timely and relevant challenge. Recent advances in computers have enabled the prediction of atomizer performance with greater accuracy, speed, and at lower cost than ever before. Fully-resolved direct numerical simulations, i.e. simulations that directly account for all relevant scales in the flow, are now possible on massive parallel computing clusters for academic and research purposes; however, computational cost remains prohibitively expensive for the widespread implementation in industry.

Similarly, advances in optical methods have improved droplet sampling (size and velocity) in the disperse regions and yielded greater insight into the core structure; yet, obtaining droplet statistics arising purely from primary breakup remains challenging due to the optically dense nature of many sprays and an inability to completely remove the influences of secondary breakup, collisions, and coalescence. Nevertheless, phenomenological correlations arising from these experiments have been invaluable in predicting overall trends and have led to numerous atomizer advances.

Numerical models that are founded on solid physics-based governing equations but do not explicitly resolve all scales of atomization offer an excellent compromise between DNS and phenomenological correlations. Models offer greater physical insight into the breakup mechanisms than correlations, but are computationally inexpensive and therefore much more approachable than DNS in industry.

The classical approach to spray modeling is through the Eulerian-Lagrangian description of two phase flows. The carrier gas phase is represented in an Eulerian reference frame and is governed by the Reynolds-averaged Navier-Stokes equations. The droplets are represented in a Lagrangian reference frame, and the resulting droplet distribution function evolution is indirectly solved using computational particles. Secondary breakup is easily modeled using computational particles in this approach. Significantly more challenging is the treatment of the primary breakup process, where the parent liquid structure is the continuous liquid core and the child structures are the discrete droplets. To avoid this obstacle, many modelers have adopted the method of injecting an assumed drop-size distribution (often chi-squared), or large mono-disperse droplets into the system to replace the primary breakup process (Reitz 1987, Huh and Grosman 1991, Arcoumanis et. al. 1997).

Unfortunately, the mechanisms responsible for primary breakup are not explicitly modeled; rather, they are replaced by simplified instability mechanisms and adjustable constants. Today, this method is known to be inadequate as the initial nozzle flow conditions (turbulence, cavitation, etc.) have been shown to greatly influence overall atomization (Baumgarten, 2002).

1.2 Objectives

The goal of the ESE model is to introduce an improved model for the primary breakup of turbulent liquid jets that considers the energy spectrum of turbulence, a physics-based drop formation criterion consistent with experimental results, and naturally brings in dependencies on Reynolds and Weber number to predict droplet statistics and size distributions. The goal of this study is to apply the ESE model to diesel sprays, demonstrate capability, and establish credibility through rigorous validation and investigative tests.

CHAPTER 2. LITERATURE REVIEW

Over the years, much research effort has gone into characterizing atomizer performance in the hopes of gaining further insight into the mechanisms responsible for primary breakup. This section focus on the literature most relevant to the ESE model and its validation, namely that which pertains to pressure atomized turbulent primary breakup of full-cone liquid jets exiting from a plain orifice into quiescent air.

2.1 Experiments

To validate a given model, some sort of quantitative representation of the drop-size histogram must be made. Direct quantifiable comparison is possible between two distributions by use of Euclidean norms; however, in the interest of brevity, it is often advantageous for authors to represent their experimental findings in a manner that is more concise yet still illustrates relevant trends and correlations. The two most common methods of representing drop-size histogram data is by computing a mean droplet diameter or by matching to some established distribution function.

If the first option is chosen, then several methods exist in which one could obtain a mean diameter. A few examples of representative diameters include the length-based (D_{10}), surface-area-based (D_{20}), and volume-based (D_{30}) mean diameters. Each of these diameters have unique and specific applications to sprays, and are reviewed further in Lefebvre (1989, p.91). By far, the most popular statistically averaged representation is the Sauter Mean Diameter, abbreviated as SMD or D_{32}. D_{32}, which is defined as the diameter of a drop that has the same volume-to-surface ratio as that of the total spray,

$$D_{32} = \frac{\sum N_i d_i^3}{\sum N_i d_i^2} \quad ,$$

is a particularly appealing measure of spray performance because droplet surface area and volume are of primary importance to evaporation and combustion.

The second option is to express the drop-size distribution in terms of an empirical distribution function. Several empirical functions have been proposed over the years; the most popular being Log-normal, Chi-square, Nukiyama-Tanasawa, Rosin-Rammler, and their derivatives. A summary of each of these will now be presented, with further discussions relevant to validation left until Chapter 4.

2.1.1 Phenomenological Correlations for Sauter Mean Diameter

A large number of SMD correlations for pressure atomized sprays have been proposed over the years. The most common input parameters are liquid density (ρ_L), gas density (ρ_G), liquid viscosity (ν_L), surface tension (σ), bulk nozzle velocity (U), Reynolds number (Re), liquid Weber number (We_L), and gas Weber number (We_G). The dimensionless numbers are defined as follows:

$$Re = \frac{\rho_L U d}{\mu_L} = \frac{\text{'inertial'}}{\text{'viscous'}} \quad , \qquad We_L = \frac{\rho_L U^2 d}{\sigma} = \frac{\text{'inertial'}}{\text{'surface tension'}} \quad ,$$

$$Oh = \frac{\sqrt{We_L}}{Re} = \frac{\mu_L}{\sqrt{\rho_L \sigma d}} \quad .$$

Correlations based on these inputs are ‘tuned’, usually through exponent manipulation, to obtain results and trends which are consistent with observed phenomena. This allows for user-friendly, predictive expressions to be developed that do not require a complete understanding of the exact mechanisms triggering the phenomenon. The danger in this is

that the complete picture of the physics of the problem is not revealed within the correlation, and thus special attention must be paid to understand the context in which the correlation was originally developed for. Therefore, in addition to listing the most popular correlations, a detailed review of the ranges of validity for each will also be presented, with implications relevant to the validation tests presented later in Chapter 4.6.

2.1.1.1 Elkotb (1982)

The 1982 correlation of Elkotb is:

$$SMD = 6156\ \nu_L^{0.385}\left(\sigma\ \rho_L\right)^{0.737}\rho_G^{0.06}\ \Delta P_L^{-0.54}$$

Notably, Ejim et. el (2007) used this correlation to demonstrate the influence of various biofuel blends on SMD, having experimentally determined there fluid properties. The correlation was reported to be valid over the following parameter ranges: $8.1x10^{-5} \leq \nu_L \leq 8.6x10^{-6}$ m^2/s, $0.0204 \leq \sigma \leq 0.0275$ N/m, $732 \leq \rho_L \leq 847$ kg/m^3, $1.20 \leq \rho_G \leq 8.20$ kg/m^3, $89 \leq (\rho_L/\rho_G) \leq 706$, and $78 \leq \Delta P_{Line} \leq 200$ bar. Where, ΔP_{Line} is the difference between injection line pressure and the gas pressure in the combustion chamber.

2.1.1.2 Varde et. al. (1984)

The 1984 correlation given by Varde, Popa, and Varde is:

$$SMD = 8.7\ d_0\ (Re_L\ We_G)^{-0.28}$$

The correlation was developed from experiments conducted on plain orifice nozzles of diameter $d_0 = 230$ μm, discharging into quiescent nitrogen gas at standard temperature and pressure. The droplet data was collected exclusively in the 'mixing region of the spray', i.e. droplets surrounding the liquid core. If x_{LC} is the length of the intact liquid core, then the

dimensionless axial range of applicability is $0 < x/d_0 < x_{LC}/d_0$. The liquid was No.2 diesel fuel, $(\rho_L/\rho_G) \approx 687$, injected at pressures: $60 \leq P_L \leq 140$ MPa.

2.1.1.3 Hiroyasu et. al. (1974)

Hiroyasu and Kadota (1974) presented the correlation:

$$SMD = 23.9\ \Delta P_{inj}^{-0.135}\ \rho_G^{0.121}\ Q^{0.131}$$

resulting from experiments conducted on diesel sprays in high-pressure gasses using the liquid immersion method for droplet capture. Where ΔP is the mean effective pressure drop across the nozzle in MPa and Q is the fuel discharge volume from pump, reported to be 35-140 mm^3/stroke. The experiment setup in which the correlation was modeled after, called for 3 plain orifice nozzles, with d_0 = 0.2, 0.25, 0.3, 0.5 mm and 9.9 MPa opening pressure, discharging into quiescent nitrogen gas at 20-25°C and 0.1-5.0 MPa. The liquid was a special diesel fuel oil at 20°C ($\nu_L \approx 2.5x10^{-6}$ m^2/s, $\rho_L \approx 840$ kg/m^3, $\sigma \approx 0.0295$ N/m). Samples were collected at $37 \leq x/d_0 \leq 373$.

2.1.1.4 Martinelli et. al. (1984)

Martinelli, Bracco, and Reitz (1984) proposed the correlation:

$$SMD = 12\ C_a\ \pi \left({}^{\sigma}/_{\rho_G\ U^2} \right) ,$$

where C_a is a drop size constant = 0.86. This correlation is not well suited for comparison with ESE for two reasons. First, the correlation was developed for systems where aerodynamic effects cannot be neglected since $13.7 \leq (\rho_L/\rho_G) \leq 39$. Second, collisions and coalescence influences are included in this correlation due to the sampling location $300 \leq x/d_0 \leq 800$, which is far beyond the liquid core length. The authors note that, "due to the

rapid entrainment, the structure of these sprays becomes dominated by the ambient gas within distances of the order of hundreds of nozzle diameters" (p. 509). Additional information regarding this correlation includes: plain orifice in quiescent gas, T = 273 k, d_0 = 100 – 300 μm, and U ≈ 100 m/s. Note that it is questionable whether this correlation is valid for modern diesel injectors since the reported velocity is significantly less than what is found in modern injectors and that the correlation has a U^2-dependence.

2.1.1.5 Faeth et. al, turbulence (1995)

The 1995 turbulence-based SMD correlation of Faeth et. al. stems from extensive research into the structure of intact liquid cores and there subsequent breakup. The correlation put forth is concisely represented by:

$$SMD = 0.65\, d_0 \left({}^{x}/_{d_0}\ We_L^{-1/2} \right)^{2/3}$$

where (x/d_0) is the dimensionless axial distance from the nozzle. The (x/d_0) dependence comes from Faeth's observations that SMD of primary droplets tends to increase with nozzle displacement along the liquid core. For this reason, (x/d_0) is valid only within the limits of the liquid core, $0 \leq x/d_0 \leq (x_{LC}/d_0)$. The experimental data from which the correlation was developed was collected over the dimensionless number range: $1x10^3 \leq We_L \leq 3x10^5$ and $1x10^3 \leq Re_L \leq 5x10^5$. Finally, it should be noted that since gas density does not appear in the correlation, the correlation should only be applied when aerodynamic effects are negligible. Faeth estimates this to be when $(\rho_L/\rho_G) > 500$, which corresponds to sprays discharging into atmospheric gas densities.

2.1.1.6 Faeth et. al, aero enhanced (1995)

In addition to the pure turbulence-based model, Faeth et. al. also introduced an improved SMD correlation to account for cases when gas density was greater than atmospheric. Specifically, Faeth found that when $(\rho_L/\rho_G) \leq 500$, such is the case for 'diesel-like' conditions, the effects of aerodynamics could no longer be neglected.

$$SMD = \left(\sigma/(\rho_G U_0^2)\right)\left(x/d_0\right)^{1/3}\left(\rho_G/\rho_L\right)^{3/4}\left(We_L^{5/6}/Re_L^{1/2}\right)$$

Like the turbulence-based, the aerodynamically enhanced correlation is also only valid for axial distances from the nozzle less than the length of the liquid core, $0 \leq x/d_0 \leq (x_{LC}/d_0)$, and was formulated from experimental results in the range of $1x10^3 \leq We_L \leq 3x10^5$ and $1x10^3 \leq Re \leq 5x10^5$.

2.1.2 Representing Drop-size Distributions

Four methods of representing drop-size distributions are presented in this section: the Chi-square, Log-normal, Nukiyama-Tanasawa, and Rosin-Rammler distributions. While all methods do indeed represent drop-size distributions, the Chi-square distribution tends to differs from the other two in its implementation. The Log-normal, Nukiyama-Tanasawa, and Rosin-Rammler distribution functions are curve-fitting techniques developed by experimentalists to quantify distribution results in a concise manner. The Chi-square distribution is usually not thought of as a tool to fit experimental data, but rather as an initial condition for use in evaporation and combustion models where initial droplet sizes are required.

The two most popular ways to report drop-size histograms is on a (frequency) number-basis or a volume-basis. Unless explicitly stated, all distributions reported in this study are number-based. That is:

$$f_N(d) = \text{number-based drop-size distribution (unscaled)}$$

$$\langle N \rangle \equiv \int_0^\infty f_N(d)\, dd = \text{total expected number of droplets}$$

$$f_R(d) \equiv \frac{f_N(d)}{\langle N \rangle} = \text{Normalized number-based probability density function}$$

$$F_N(d) = \text{Cumulative number-based drop-size distribution function}$$

$$f_N(D) \equiv \frac{dF_N(d)}{dd}$$

2.1.2.1 Chi-square

The Chi-square distribution is perhaps the simplest technique for representing drop-size distributions. In KIVA, one option available is to perform random sampling of the Chi-square distribution in place of breakup models, which is then input into subsequent evaporation and combustion routines. This distribution is

$$f_N(r) = \frac{1}{\bar{r}} \exp\left(-r/\bar{r}\right)$$

where

$$\bar{r} = \frac{1}{3} r_{32} = \frac{1}{6} d_{32} \ .$$

As can be seen, the distribution depends solely on SMD, and thus does not allow for variations in distribution variance with fixed SMD.

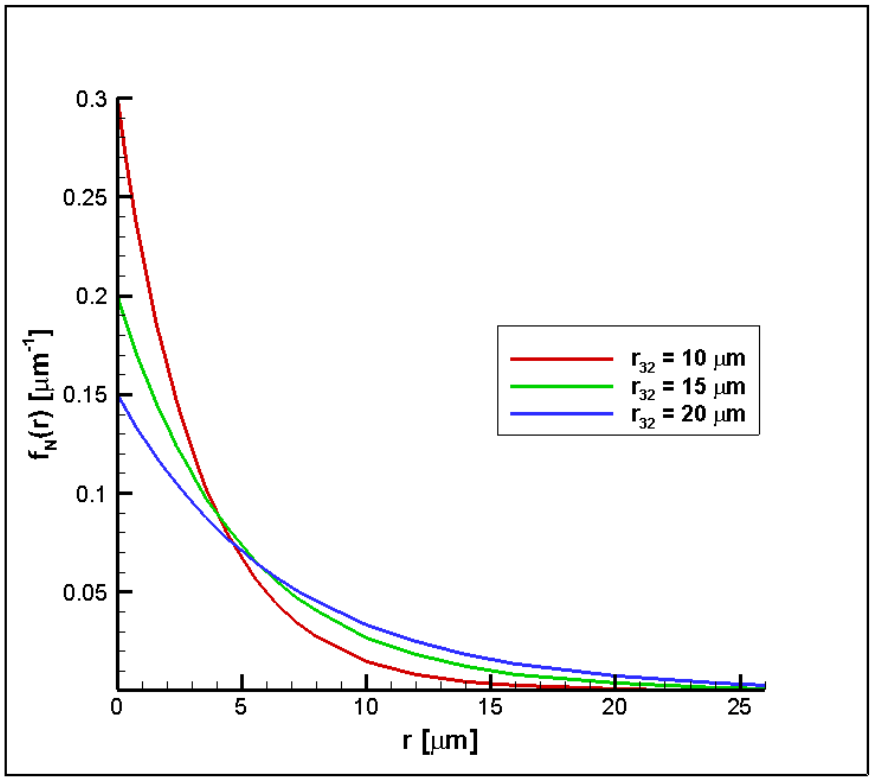

Figure 2.1. Typical Chi-square distributions for $f_N(r)$

2.1.2.2 Log-normal

The Log-normal distribution is,

$$f_N(d) = \frac{1}{d(\ln(\sigma_{LN}))\sqrt{2\pi}} \exp\left(-\frac{1}{2}\left[\frac{\ln\left(d/\bar{d}\right)}{\ln(\sigma_{LN})}\right]^2\right) \quad ,$$

where $\bar{d}$ and σ_{LN} are the logarithmic mean diameter and width of the distribution, respectively. The advantage of this distribution is that it has two adjustable parameters, thereby allowing both mean and variance to be adjusted independently. This feature allows the Log-normal to be able to represent a greater range of distributions encountered by various atomizer designs.

2.1.2.3 Nukiyama-Tanasawa

The Nukiyama-Tanasawa distribution's advantage over Chi-square is a much better representation of the small diameter drops. Comparison of Figures 2.1 and 2.2 shows that Chi-square predicts the single most likely drop-size to be that having zero diameter, while Nukiyama-Tanasawa correctly predicts zero probability of forming zero diameter drops. Indeed, inspection of the Wu and Faeth criterion (1995) for drop formation,

$$\rho_L v^2 \geq \frac{12\ C_L\ (4\pi\ d^2)\ \sigma}{\pi\ d^3} \quad ,$$

reveals that it would take infinite kinetic energy to form a zero diameter drop.

The disadvantage of this distribution is a larger number of model constants required relative to other curve-fitting techniques. The Nukiyama-Tanasawa distribution has the form:

$$F_N(d) = a\ d^p\ \exp(-b\ d^q) \quad ,$$

where a, b, p, and q are the four independent model constants. Following Sojka (2002) and Lefebvre (1989), it is common practice to fix parameter p at 2. Figure 2.2 shows that the combination of parameters b and q are responsible for droplet spread and mean diameter. Finally, parameter a is a normalizing constant.

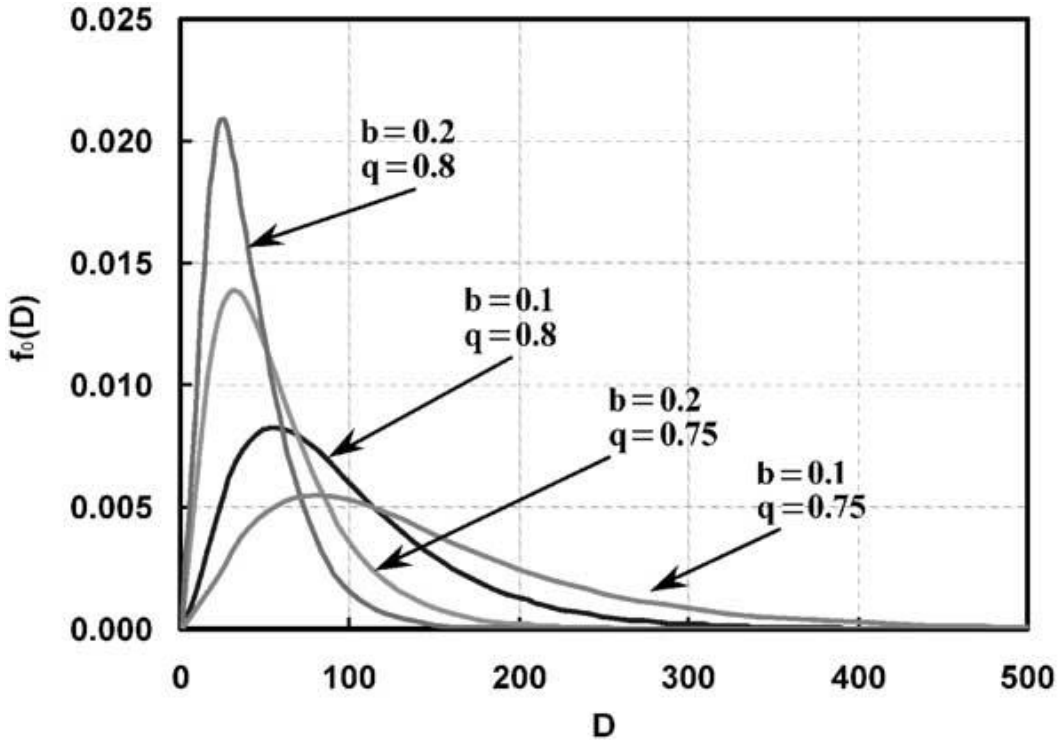

Figure 2.2. Typical Nukiyama-Tanasawa distributions for $f_N(d)$ (Sojka, 2002)

2.1.2.4 Rosin-Rammler

The Rosin-Rammler distribution was originally developed in 1933 for the representation of coal particulates, but has since seen widespread implementation into the field of liquid atomization (aerosols). This distribution's high popularity can be attributed to its simplicity as seen when expressed as a cumulative volume distribution,

$$F_V(d) = 1 - \exp\left(-\left(d/X\right)^q\right) \quad ,$$

or as a number distribution,

$$f_N(d) = qX^{-q}d^{q-1}\exp\left(-\left(d/X\right)^q\right) \quad .$$

Unlike the Nukiyama-Tanasawa distribution, Rosin-Rammler requires just two model constants, X and q, where X is the characteristic drop diameter representing 63.2% of the total liquid volume contained in drops of smaller diameter and q is a measure of drop-size

uniformity. According to Lefebvre (1989), typical pressure atomizers have q-values between 1.5 and 4, with larger values representing less drop-size spread.

2.2 Breakup Models

Typical breakup models fall somewhere between fully-resolved DNS and phenomenological correlations in terms of complexity and comprehensiveness. Breakup models replace the resolution requirements faced in DNS with some simplified computationally tractable representation, often referred to as a sub-model. The advantage models hold over empirical phenomenological correlations, is a greater insight into the physics responsible for breakup. The consensus among spray scientists is that there are three dominant primary breakup mechanisms: aerodynamic, turbulent, and cavitation induced. Most breakup models may be sub-classified as one of these three, or some combination thereof.

2.2.1 Aerodynamic Models

The 'blob' method, developed by Reitz (1987), is the one of the most popular breakup models for high speed pressure atomizers used today. While technically a secondary breakup model, the blob method is often employed as a semi-complete representation of the atomization process as a whole. In simplest terms, the blob method is the application of the Kelvin-Helmholtz instability mechanism found in the 'Wave-breakup model' to mono-disperse droplets with diameters comparable to the size of the nozzle. The initial large mono-disperse droplets injected into the system, called 'blobs', replace the initial breakup of

the intact liquid core on the basis that primary and secondary processes are assumed indistinguishable within the dense liquid region.

The ‘blobs’, or ‘parent droplets’, are injected into the model at a rate governed by the mass flow rate, ṁ. Small secondary, child droplets are sheared off of the parent with size:

$$r_{child} = B_0 \, \Lambda \quad \left(\text{if } r_{child} \leq r_{parent}\right) ,$$

where $B_0 = 0.3 + 0.6P$ and P is a random number (0,1]. Λ is the wavelength corresponding to the fastest growth rate, Ω, given by:

$$\Lambda = 9.02 \, r_{parent} \frac{\left(1 + 0.45 \, Z^{0.5}\right)\left(1 + 0.4 \, T^{0.7}\right)}{\left(1 + 0.87 \, We_G^{1.67}\right)^{0.6}} ,$$

where We_G is the gas Weber number:

$$We_G = \frac{\rho_G \, U^2 d_{droplet}}{\sigma} = \frac{\text{'inertial'}}{\text{'surface tension'}}$$

Z is the Ohnesorge number:

$$Z = Oh = \frac{\sqrt{We_L}}{Re} = \frac{\mu_L}{\sqrt{\rho_L \sigma d_{noz}}}$$

and T is the Taylor number:

$$T = Z \sqrt{We_G} .$$

In cases of low speed breakup, it is possible for droplets to be formed that are larger than the nozzle diameter. For this condition, when the child droplet is larger than the parent, r_{child} becomes:

$$r_{child} = \min \begin{Bmatrix} \left(3 \, \pi \, r_{parent}^2 \, U_0 \, / \, (2 \, \Omega)\right)^{1/3} \\ \left(3 \, r_{parent}^2 \, \Lambda \, / \, 4\right)^{1/3} \end{Bmatrix} .$$

The final step is to update the parent drop diameter on the basis of mass removed due to child droplets:

$$\frac{dr_{parent}}{dt} = -\left(\frac{r_{parent} - r_{child}}{\tau}\right) \quad ,$$

where τ is the breakup time scale given by:

$$\tau = 3.726\, B_1\, \frac{r_{parent}}{\Lambda\, \Omega}$$

Ω is the fastest growth rate:

$$\Omega = \frac{0.34 + 0.38\, We_G^{1.5}}{(1+Z)\,(1+1.4\,T^{0.6})} \left(\frac{\sigma}{\rho_L\, r_{parent}^3}\right)^{0.5}$$

and B_1 is an inner nozzle flow constant between 1.73 and 30.

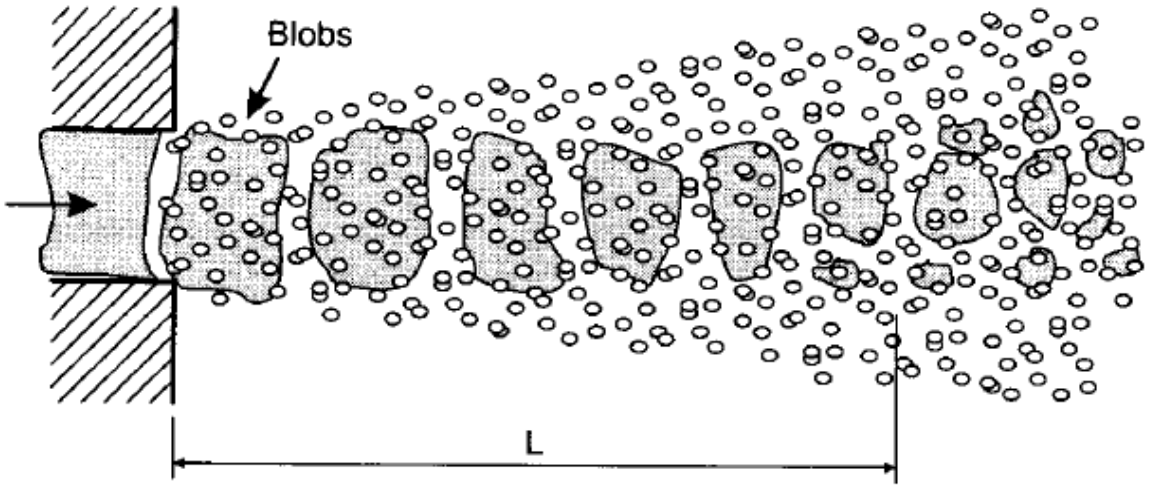

Figure 2.3. Schematic of Blob method (Reitz, 1987)

2.2.2 Turbulence - Aerodynamic Models

Nearly all recent turbulence based breakup models have been developed as modifications or extensions of the Kelvin-Helmholtz aerodynamic instability mechanism.

The combined phenomenological model of Huh and Gosman (1991) is a good, typical example of this trend.

Analogous to the blob method, this model starts by injecting mono-disperse droplets with diameters equal to that of the injector nozzle. Initial instabilities on the parent droplet are created corresponding to the most unstable surface waves, taken to be proportional to a supposed characteristic atomization length scale, L_A,

$$L_A = C_1 L_t = C_2 L_w$$

where $C_1 = 2.0$, $C_2 = 0.5$, L_t = turbulence length scale, and L_w = surface perturbation wavelength. The turbulence length scale is determined by the averaged turbulent kinetic energy, dissipation rate, and a constant arising from the k-ε-model, denoted k, ε, and C_μ respectively.

$$L_t = C_\mu \frac{\kappa^{1.5}}{\varepsilon}$$

The turbulence-induced instabilities then grow due to aerodynamic interactions represented by the Kelvin-Helmholtz mechanism.

2.2.3 Combined Cavitation Models

While the effects of cavitation are known to influence drop-size distributions and spray angles, cavitation models are typically not developed to be stand-alone models. There is a tendency for new cavitation models to be coupled with one or both of the other breakup mechanisms.

Nishimura and Assanis (2000) proposed a model for cavitation and turbulence. The model is applied to cylindrical ligaments with diameters equal to that of the injector nozzle. Turbulent kinetic energy increases due to bubble collapse, with the reduction in volume

given by Rayleigh's theory of bubble dynamics. Other models such as those developed by Baumgarten (2002) and Arcoumanis et. al. (1997) included the effects of all three mechanisms.

CHAPTER 3. THE ESE MODEL

3.1 Conceptual Basis for the Model

In this chapter the fundamental theory underlying the ESE model, governing equations, and their integration into engine simulations will be discussed. First, it is necessary to illustrate the conceptual framework upon which the model is based.

The ESE is a spectral model, i.e. it considers the energy contained within the full range of turbulent eddies present in the flow. The total energy spectrum, E_t, is often plotted against wavenumber, k. Wavenumber is defined as the inverse of the fluctuating wavelength, λ, giving it units of $[L^{-1}]$. Thus, plotting E_t versus k gives the density of turbulent kinetic energy (TKE) over all the scales of the flow. The energy spectrum of pipe flow was chosen for this model, as it is the closest known analogue to the nozzle geometry.

Knowing the range of eddies allows for the use of the well known Wu and Faeth (1995) drop formation mechanism:

$$\rho_L v_L^2 \left(\frac{\pi\lambda^2}{12}\right) \geq C_L \left\{4\pi \left(\frac{\lambda}{2}\right)^2 \sigma\right\}$$

which is an essential tenet of the ESE model. The mechanism says that a droplet will only be formed if the turbulent kinetic energy of an eddy of size λ must exceed the surface energy of a droplet having equivalent diameter. The velocity fluctuations in the kinetic energy term attempt to break apart the liquid core while the surface tension attempts to maintain it. To use this formation mechanism, it is assumed in the ESE model that droplet size is equal to the size of the eddy from which it was formed:

$$\lambda = 1/k = d_{droplet} \ .$$

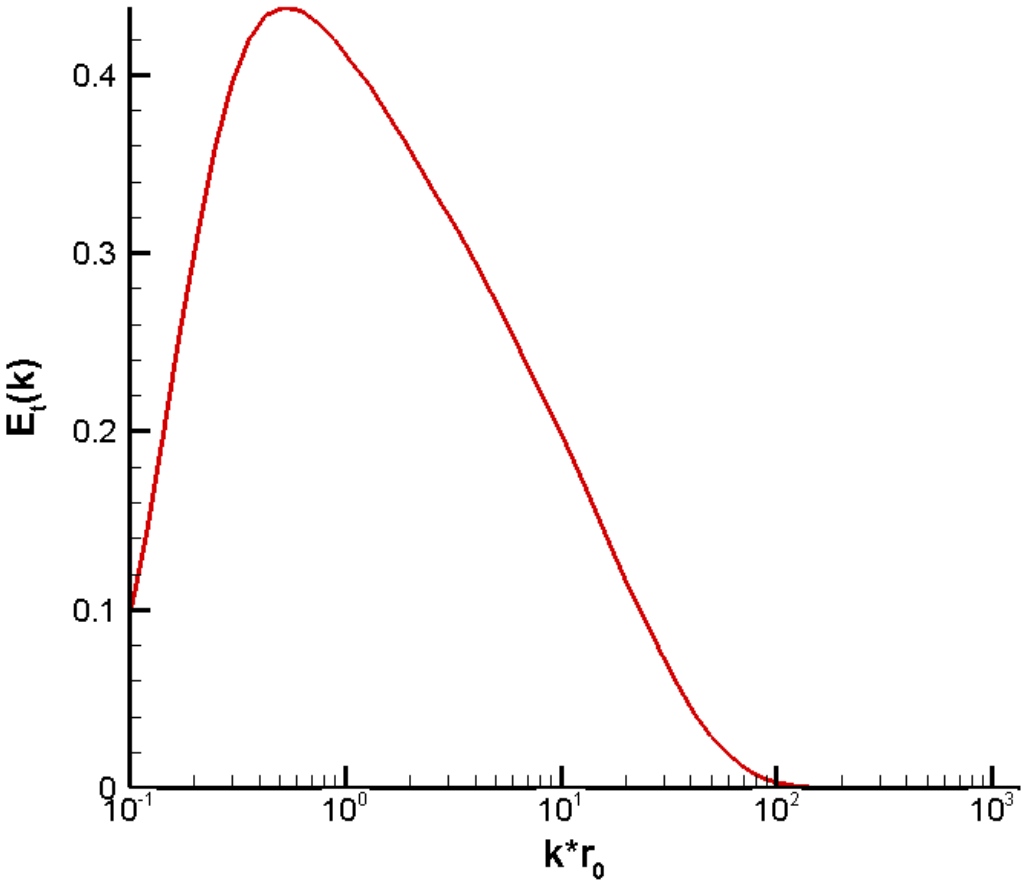

Figure 3.1. Example of pipe flow energy spectrum

3.2 Model Formulation

The energy spectrum, E_t, is derived for homogeneous, axisymmetric turbulence to represent pipe flow, with dependencies on wavenumber, k, and cosine angle, μ. The cosine angle is formed from the jet symmetry line and is necessitated by the discrepancies in axial ($\mu = 1$) and transverse ($\mu = 0$) fluctuations present in axisymmetric flows. Following Chandrasekhar (1950) the representation of the two point velocity correlation tensor for axisymmetric turbulence is defined in terms of two scalar functions, E and F, having the form:

$$E_t(k,\mu) = E(k,\mu) + \frac{1}{2}(1-\mu^2)\, F(k,\mu) \quad .$$

The well-known 1-dimensional spectra, E_{11} and E_{33}, may be expressed in terms of the spectrum functions, E and F, by:

$$E_{11} = \frac{1}{4} \int_0^1 \{E(k,\mu) + \mu^2 \,[E(k,\mu) + (1 - \mu^2)\, F(k,\mu)]\}\, d\mu$$

$$E_{33} = \frac{1}{2} \int_0^1 (1 - \mu^2)\,[E(k,\mu) + (1 - \mu^2)\, F(k,\mu)]\, d\mu$$

The equilibrium evolution equations for E and F are derived from the turbulence model of Canuto and Dubovikov (1996), yielding the following expressions:

$$\left[\frac{\partial E(k,\mu,t)}{\partial t}\right]_{eq} = A_l^t(k) + 2k^2 \nu_{d0}(k)\, E(k,\mu,0) - A_{l0}^t(k) - 2\, k^2\, \nu_d(k)\, E(k,\mu,t)$$

$$\left[\frac{\partial F(k,\mu,t)}{\partial t}\right]_{eq} = 2k^2 \nu_{d0}(k)\, F(k,\mu,0) - 2\, k^2\, \nu_d(k)\, E(k,\mu,t)$$

$$A_l^t(k) = -\frac{\partial \pi}{\partial k} + 2k^2\, \nu_t(k)\, E_t(k,t) = \text{'work by turbulent forcing'}$$

$$T_l(k) = -\frac{\partial \pi}{\partial k} \equiv \text{'spectral energy transfer term'}$$

$$\pi = 2E_t\Omega = 2E_t(k) \int_0^k k^2 \nu_t(k) dk$$

In the absence of additional terms the spectrum is stationary and relaxes to that of pipe flow. Energy is drawn from the mean flow, cascades from the large eddies to the small, and is finally dissipated by viscous effects. However, an additional term is used in the ESE model: energy is drawn from the equilibrium spectrum through sink terms, S_{Ed} and S_{Fd}, corresponding to droplet formation:

$$\frac{\partial E(k,\mu,t)}{\partial t} = \left[\frac{\partial E(k,\mu,t)}{\partial t}\right]_{eq} + S_{Ed}(k,\mu,t)$$

$$\frac{\partial F(k,\mu,t)}{\partial t} = \left[\frac{\partial F(k,\mu,t)}{\partial t}\right]_{eq} + S_{Fd}(k,\mu,t)$$

The E and F sink terms are:

$$S_{Ed}(k,t) = -\frac{4}{\tau_d}\left\{E_{11}(k,t) - \left[\frac{E_{11}(k,t_o)}{E_d}\right]\cdot E_d\right\} H[E_{11}(k,t) - C_t E_{11}(k,0)]\{H[t - t_o(k)] - H[t - t_o(k) - \tau_d(k)]\}\, H[d_c(k) - 1/k]$$

$$S_{Fd}(k,\mu,t) = -S_{Ed}(k,\mu,t)$$

Where C_t is a model constant that limits the energy drawn by the sink term such that the energy spectrum is always non-negative and $t_0(k)$ is the time at which the sink is activated at a given wavenumber. E_d is the minimum specific energy density per wavenumber to form a droplet, which when rendered dimensionless takes the form:

$$\overline{E}_d(k) = \frac{C_{df}}{We_L}\left(\frac{u'}{U_0}\right).$$

The ratio $\left[\frac{E_{11}(k,t_o)}{E_d}\right]$ represents the maximum possible number of integer drops formed at t_0.

The purpose of E_d is twofold. First, the criterion ($E_{11}(k,t_0) > E_d$) determines if enough energy exists at a given wavenumber and time to initiate the drop formation process. This criterion is a derivation of the Wu and Faeth (1995) drop formation mechanism presented in Section 3.1:

$$\rho_L v_L^2 \left(\frac{\pi\lambda^2}{12}\right) \geq C_L\left\{4\pi\left(\frac{\lambda}{2}\right)^2 \sigma\right\}.$$

Again, noting that the following assumption was made:

$$\lambda = 1/k = d_{droplet}\ .$$

If the first criterion is satisfied, then energy is extracted from the spectrum at a rate proportional to the drop formation timescale, τ_d, and accumulated in a reservoir term, R_{df}:

$$R_{df}(k,t) = -\frac{1}{4}\int_0^s S_{Ed}(k,t)\ dt\ .$$

The second role of E_d is an energy threshold that the accumulation of R_{df} must exceed before a drop may be formed.

The formation timescale is assumed equal to the minimum of the turbulence and Rayleigh timescales:

$$\tau_d = \tau \min\left\{1, We_L^{1/2}\left[\bar{k}^{-1/2} + 3\ Oh\ We_L^{1/2}\right]\right\} \tag{3.1}$$

$$\tau = 2\pi / \left[k^3 E_t(k)\right]^{1/2}\ . \tag{3.2}$$

Under most 'diesel-like' conditions, the turbulence timescales are faster and thus are the dominant mechanism.

Inspection of the sink terms reveals conditionality upon three additional criteria:

$$E_{11}(k,t) > C_t\ E_{11}(k,0)$$

$$t_o < t < t_o + \tau_d$$

$$1/k \leq d_c(k)\ .$$

The first ensures that the energy drawn by the sink term cannot exceed some fraction of the energy present at the time of initial sink activation. Further discussion of C_t may be found in Section 4.4.2. The second ensures that the sink is only active over the duration of the droplet formation timescale. The third criterion prevents the formation of droplets that are larger than the core cross-section. A schematic is given in Figure 3.2 to illustrate model structure and flow.

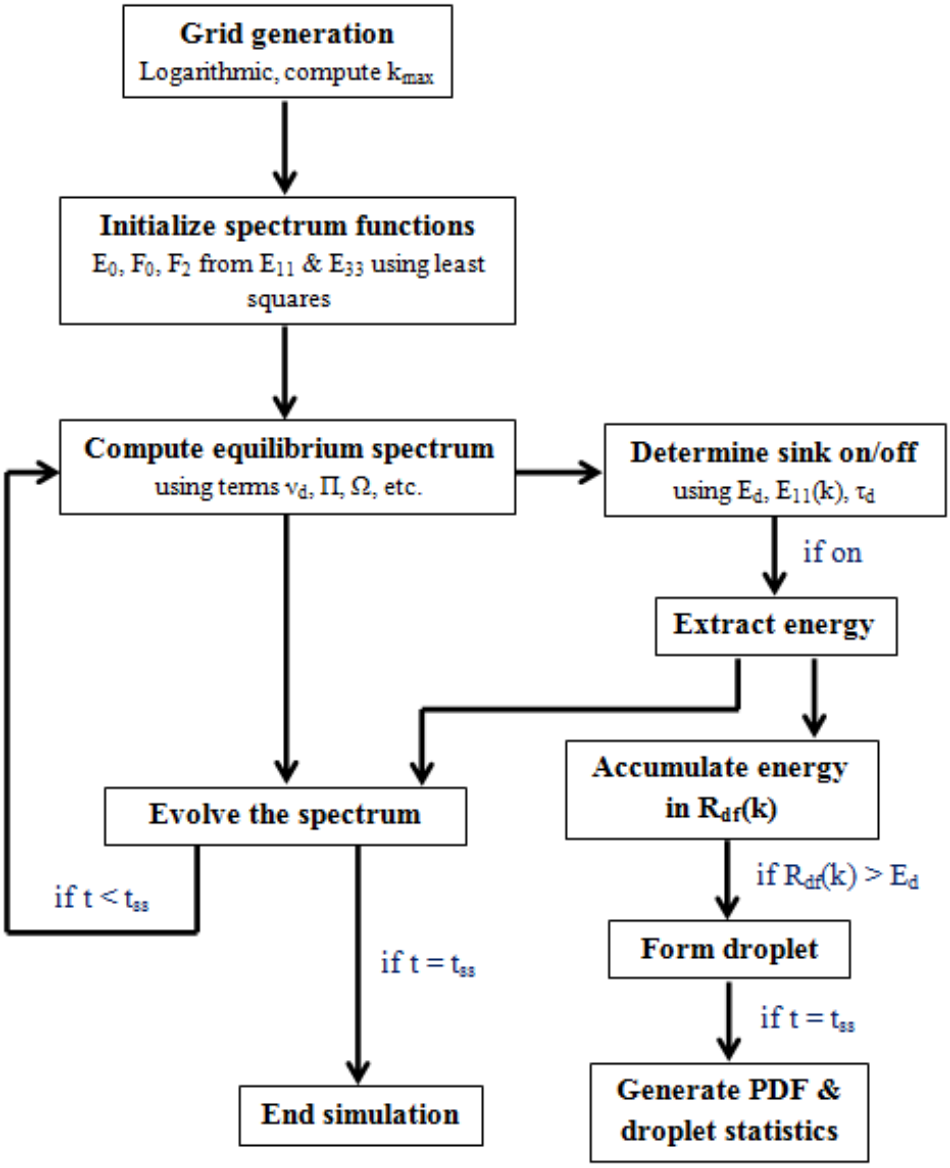

Figure 3.2. ESE model flow chart

Since ESE is a spectral model, and the length scales of turbulence may approach the size of the nozzle, i.e. the integral length scales, the model's physics do not preclude the formation of droplets on the order of the injector itself; however, experimental evidence shows that such situations do not exist under 'diesel-like conditions'. Thus, there is a need to impose some constraint on the formation of these large diameter droplets to better match experimental results. This upper limit constraint is formulated on the basis that a droplet of

diameter, $d = \lambda \equiv (1/k)$, may not exceed the diameter of the liquid core, $d_c(x)$, from where it was formed.

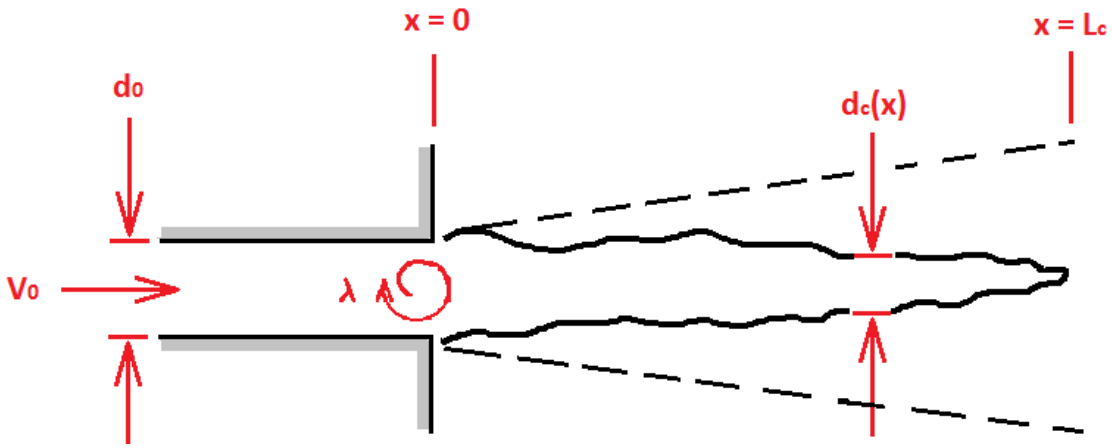

Figure 3.3. Schematic of d_c criterion

From equations 3.1 and 3.2, it is known that a droplet of diameter, $d = \lambda$, takes a finite time to form, $\tau_d(\lambda)$, and that an axial displacement associated with the formation of this droplet may be calculated if the bulk liquid core velocity, V_0, is known:

$$x_d(\lambda) = \tau_d(\lambda)\, V(x) \quad . \tag{3.3}$$

Applying the correct dimensional scaling to dimensionless $\tau_d(\lambda)$ from ESE:

$$\tau_d(\lambda) = \bar{\tau}_d(\lambda)\, \tau_{\eta_0} \ ,$$

where

$$\tau_{\eta_0} = \left(\nu/\eta_0^2\right)^{-1} = \left(\frac{\nu}{(\nu^3/\varepsilon)^{1/2}}\right)^{-1} = \left(\frac{\nu}{\varepsilon}\right)^{1/2} \ .$$

The variables η and ε are the Kolmogorov length scale and the rate of dissipation of turbulent kinetic energy, respectively. Typical nozzle velocities, V_0, range between 350 and 500 m/s, and the approximation $V(x) \approx V_0$ may be made with only slight loss of accuracy due to the large momentum and slow relaxation time of the liquid core (Faeth, 1995).

Next, the relationship given by Chehroudi et. al. (1985) gives an approximation for the dimensionless intact liquid core length:

$$\frac{L_c}{d_0} = C_c \left(\frac{\rho_L}{\rho_G}\right)^{1/2} \quad ,$$

where, C_c is a model constant between 7 and 16. Setting C_c to 7, we find typical (L_c/d_0) values for this study (atmospheric gas) are approximately 180, while sprays under 'diesel-like' conditions typically range from 35 to 45, depending on compression ratio.

For simplicity, the liquid core profile is assumed to decrease linearly with axial distance.

$$d_c(x) = -\left(\frac{d_0}{L_c}\right) x + d_0 \tag{3.4}$$

If this assumption proves to be inadequate, then any other simple geometric shape may be chosen in its place. Next, combining equations 3.3 and 3.4 yields,

$$d_c(\lambda) = -\left(\frac{d_0}{L_c}\right) (\tau_d(\lambda) * V_0) + d_0 \quad ,$$

where the criterion for drop formation is:

$$\lambda \leq d_c(\lambda) \quad .$$

Using this argument, we find the maximum possible droplet diameter in atmospheric gas to be 150 μm ($d/d_0 = 0.83$) and 133 μm ($d/d_0 = 0.73$) under 'diesel-like' conditions. As can be seen in Figure 3.4, the liquid-gas density ratio has a direct influence on the formation of large drops. This phenomenon is in agreement with the conclusions of Reitz (1986), in which Sauter Mean Radius was found to decrease with increased gas density due to primary breakup, but subsequently increase thereafter due to increased coalescence efficiency, an

effect not captured by the ESE model. The importance of this constraint will be discussed further in Chapter 4.

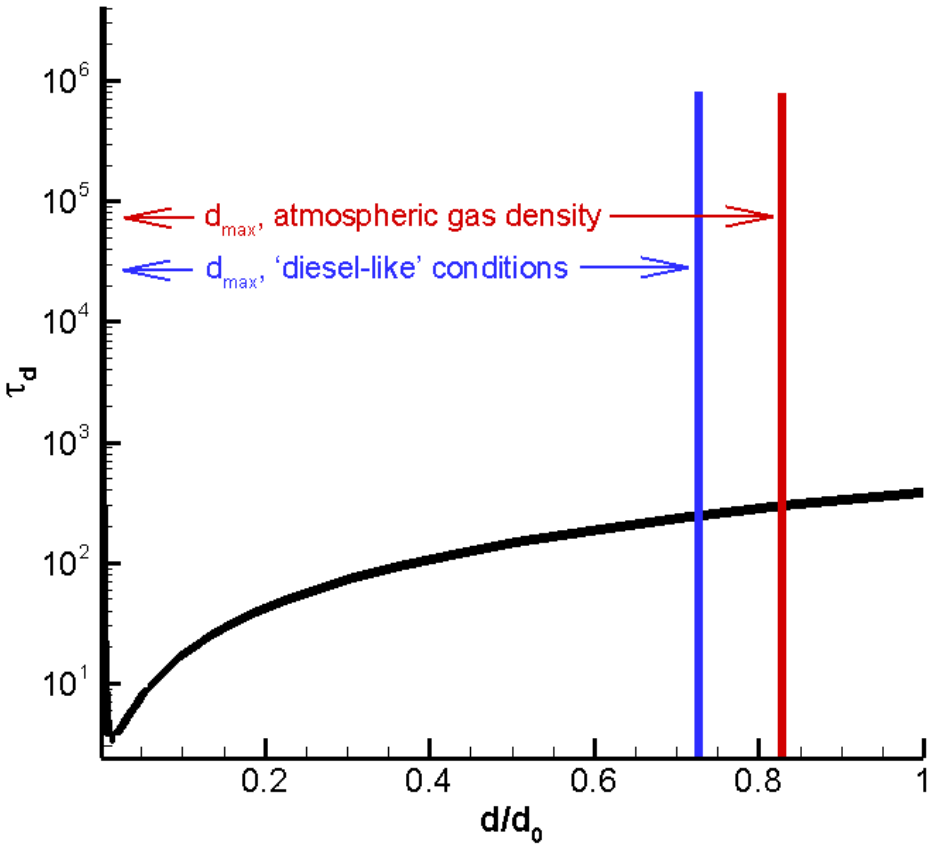

Figure 3.4. Upper drop-size limit from time scale analysis

3.3 Application to Engine Simulation

Complete engine simulation programs such as KIVA utilize subroutines to model the numerous specific processes undergone each cycle. Figure 3.5 shows an outline of the major subroutines present in a modern code, where the highlighted subroutine represents the current study's contribution. The ESE requires inputs of U, d_0, t, ρ_L, μ_L, σ, ρ_G and outputs $f_N(d)$ to the secondary routines.

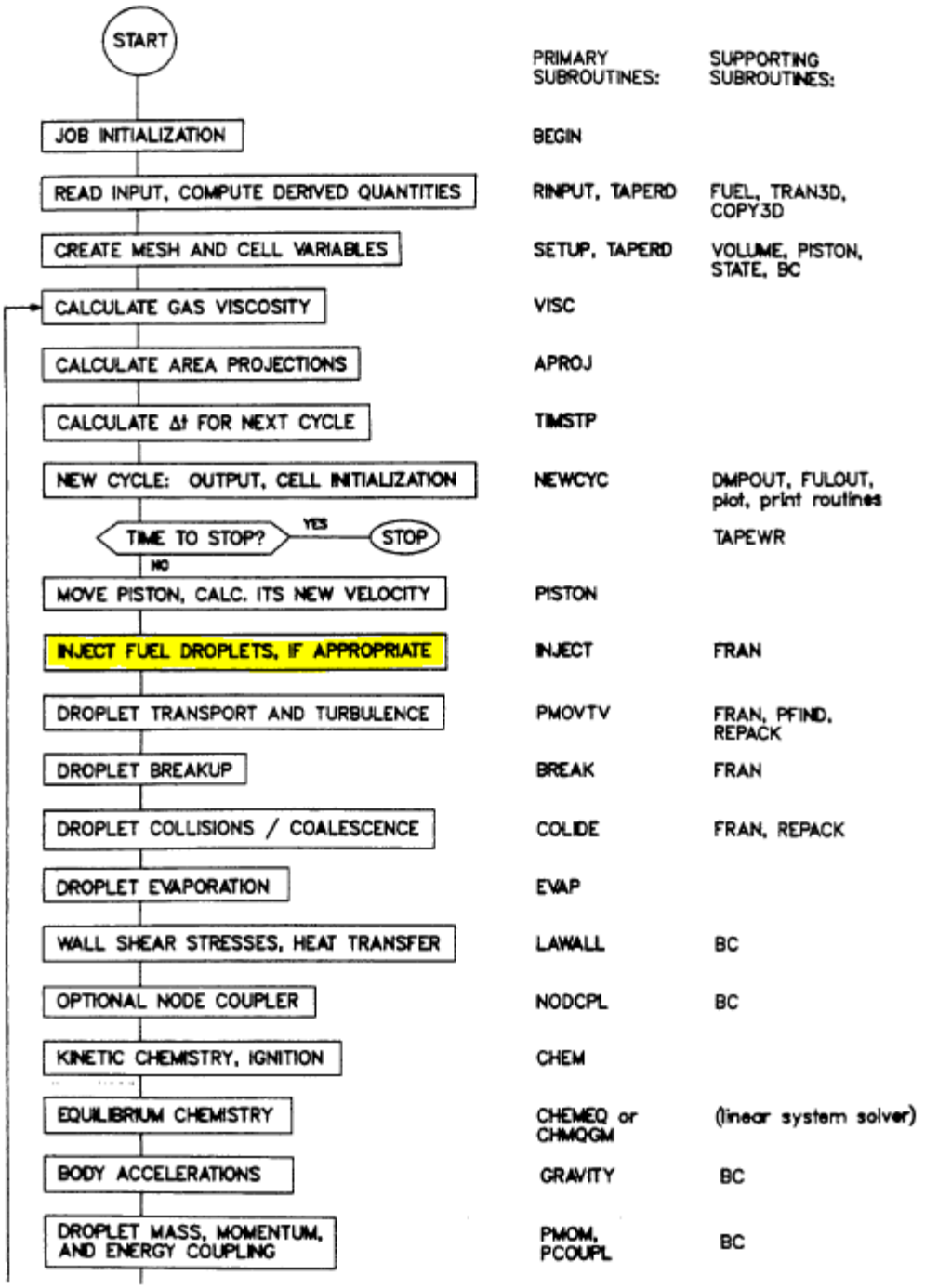

Figure 3.5. Flow chart (partial) showing ESE placement in KIVA (Amsden et. al., 1989)

CHAPTER 4. MODEL VALIDATION

4.1 Introduction

In this chapter we wish build confidence in the ESE model through rigorous validation and investigative testing. The first section outlines the special considerations taken in this investigation to ensure the best possible comparisons were made. These topics include ideal spatial sampling location, special restrictions imposed by the model, and appropriateness of using DNS and experiments to validate primary breakup models. From these discussions, 4 validation tests were conducted to demonstrate model convergence, sensitivity to model constants, variation of flow parameters, and variation of fluid properties. Finally, extensive discussions and conclusions are formulated, with several suggestions for possible future improvements to the model.

4.2 Special Considerations for Validation

4.2.1 Reynolds Number

The initial model spectra, E_{11} and E_{33}, are computed for centerline pipe turbulence from S. B. Pope given Reynolds number. The spectra are then used to initialize the functions E and F according to the equations given in Chapter 3. To calculate E and F a least-squares method is implemented to resolve the under-determined system of equations. Using this method imposes restrictions on turbulence Reynolds number, Re_{T0}, if the initial E_{11} and E_{33} spectra are to be solved exactly. It should be noted that if some finite error were tolerated in the computation of E and F, then it is possible that this restriction could be relaxed. In this

study we choose to use the former method, and thus the turbulence Reynolds number range that produces realizable E and F is found to be between 984 and 1410. The consequences of this are translated into restrictions on the bulk-flow Reynolds number by:

$$Re_{T0} = K\,Re^{*}$$

Where:

$$K = \text{Von Karrman constant} = 0.41$$

$$Re^{*} = Re_0\,\frac{u^{*}}{U_0} \quad \text{and} \quad u^{*} = U\sqrt{f/8}$$

$$U = \text{bulk velocity},\ U_0 = \text{centerline velocity},\ u^{*} = \text{friction velocity},\ f = \text{friction factor}$$

$$U_0 = \frac{3u^{*}}{2K} + U \quad \text{and} \quad Re_0 = \frac{3u^{*}d_{noz}}{2K\upsilon} + Re$$

$$\frac{1}{\sqrt{f}} = \text{-}2.0\,\log\left(\frac{\varepsilon/d_{noz}}{3.7} + \frac{2.51}{Re\sqrt{f}}\right)$$

$$\epsilon \sim 0.002\ \text{mm} = \text{equivalent roughness}$$

Thus:

$$Re_0 = \frac{Re_{T0}}{K\,\frac{u^{*}}{U_0}} \quad \longrightarrow \quad Re = \frac{Re_{T0}}{K\,\frac{u^{*}}{U_0}} - \frac{3u^{*}d_{noz}}{2K\upsilon}$$

The bulk-flow Reynolds number range is thus 25,000 to 50,000, where modern diesel injectors typically operate between 35,000 and 70,000.

Given that the ESE model is being applied exclusively to diesel fuel injection systems in this paper, the range of ‘real’ injector diameters and ‘real’ fluid properties is finite; therefore, restrictions are also imposed on the bulk velocity, U. Depending on which fuel and nozzle is chosen, the range of U allowed by the ESE can vary considerably. The constraint for pure diesel fuels is approximately 225 to 450 m/s, while some high-viscosity

pure biofuels could theoretically be simulated up to 700 m/s. As a comparison, modern high-performance diesel injectors occasionally achieve velocities in excess of 500 m/s.

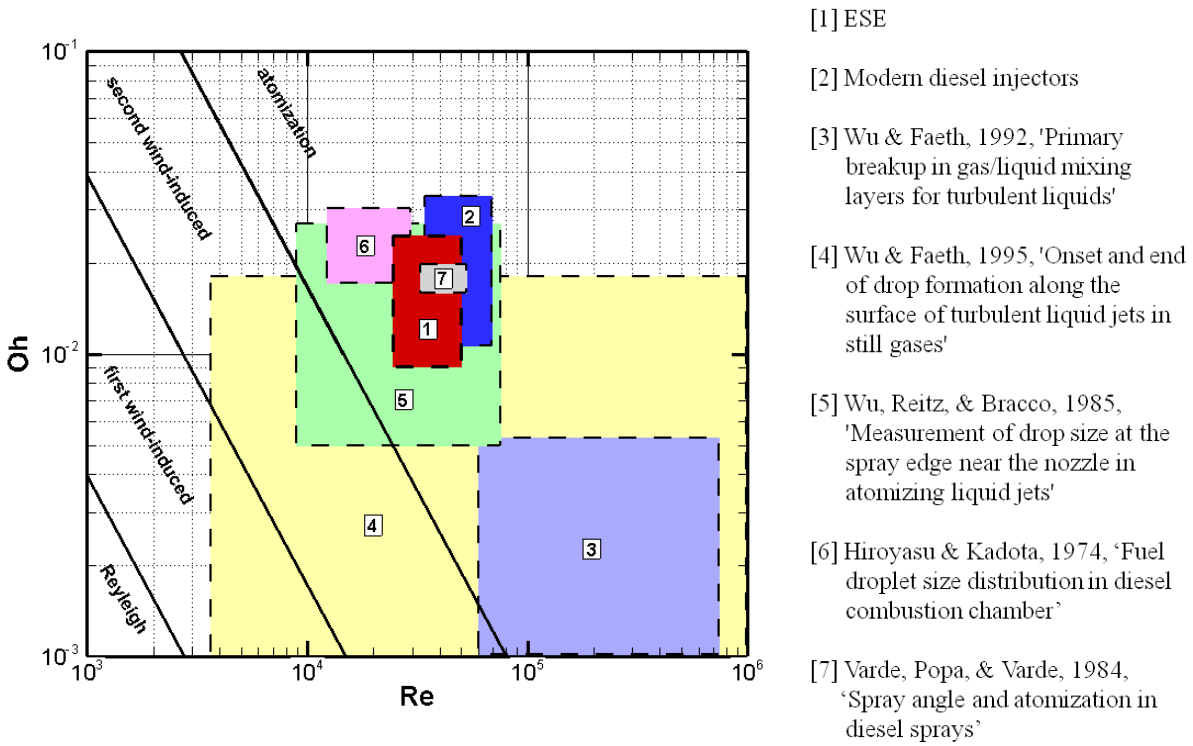

Figure 4.1. Jet operating regions

The bulk velocity restriction in turn limits the liquid Weber number range since:

$$We_L = \frac{\rho_L U^2 d_0}{\sigma} \quad .$$

The limits imposed as consequence of these restrictions, along with the range typical of modern diesel injectors and published experiments, are concisely represented on a Re versus Oh plot, shown in Figure 4.1. Two conclusions may be reached from this plot. First, the restrictions used in this study still allow the ESE to simulate many of commercially available diesel injection systems on the market today; however, in its current form one cannot achieve the dimensionless parameters of some modern high-performance systems. Second, there is a

wealth of experimental data available within this region, spanning the last four decades, for which to validate breakup models.

4.2.2 Spatial Location of Drop-size Sampling

The drop-size distributions tend to be highly dependent upon both axial and radial distances from the nozzle. For this reason, special care must be taken to ensure spatial compatibility between the reference work and the model being validated. The relative influences of these spatial parameters on the histogram, as reported in the works of J. B. Blaisot et. al. (2005) and Varde et. al (1984), are illustrated in Figures 4.2 and 4.3, respectively. As can be seen, samples taken further downstream of the nozzle tend to capture a greater proportion of large drop-sizes, thus producing a much broader PDF. This trend is understood to be the result of a combination of varying formation time scale dependent on droplet size and coalescence influences.

The ESE model is a primary breakup model, which means that it is only valid in the dense liquid region closest to the intact liquid core where droplets initially detach. The appropriate axial sampling location may be approximated via empirical correlations for intact liquid core length, given by such authors as Chehroudi et al (1985)

$$L_c/d_0 = C_c \left(\rho_L/\rho_G\right)^{1/2} ,$$

Using this correlation, typical liquid core lengths relevant to the operating conditions in this study were found to range between 150 and 400 times the nozzle diameter, or roughly 27 to 75 mm for the typical diesel injector discharging into atmospheric air densities.

Extending the study to ‘diesel-like’ conditions, the liquid core length may be as small as 8 - 20 mm, depending on compression ratio.

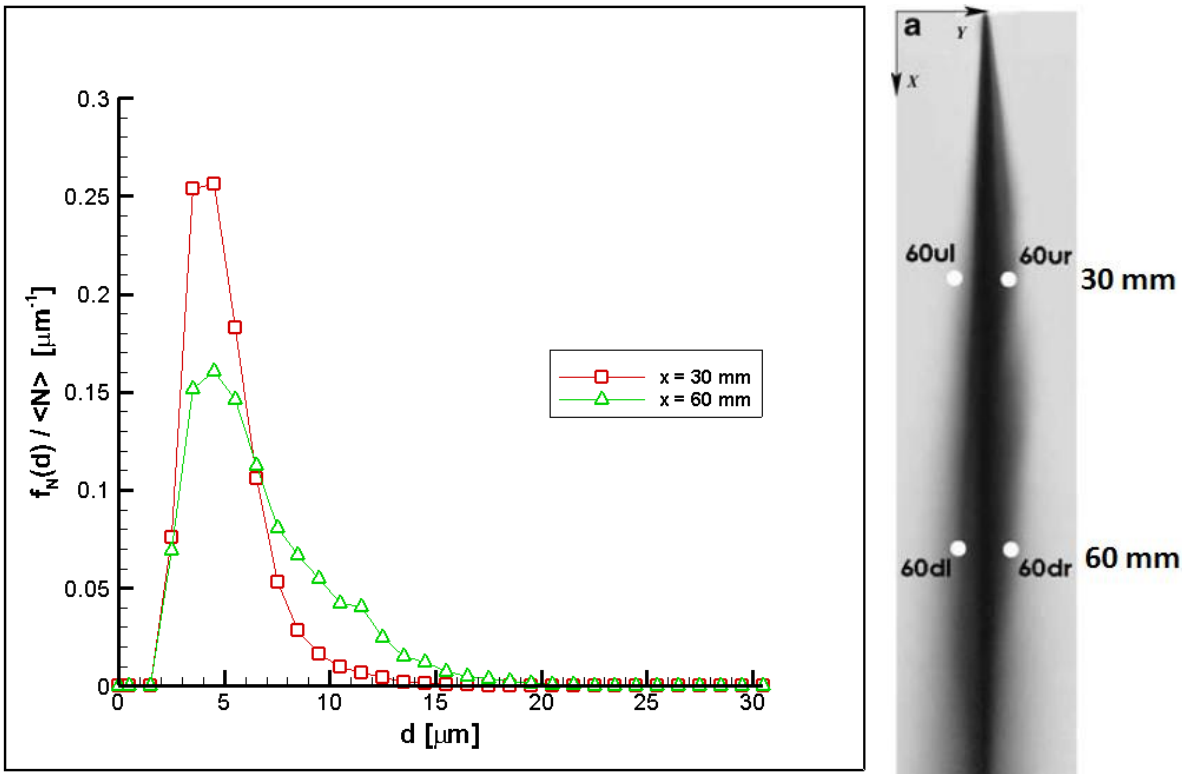

Figure 4.2. Influence of axial sampling location on PDF (Blaisot, 2005)

Ideally, the radial sampling location should be at the gas - liquid core interface so to capture the formation of primary droplets with negligible secondary breakup, collisions, coalescence, and evaporation. Indeed, Figure 4.3 clearly shows the secondary effects can drastically change the drop-size distribution in displacements as small as 5 mm. In practice however, obtaining droplet diameters at the core is exceedingly difficult, requiring ‘real-world’ samples to be taken from a compromised location where proper resolution may be achieved while still minimizing undesirable secondary processes. Using the terminology of Faeth (1995) and Figure 4.10, the region of interest is called the ‘multiphase mixing layer’ which is bounded by the liquid core and spray cone angle.

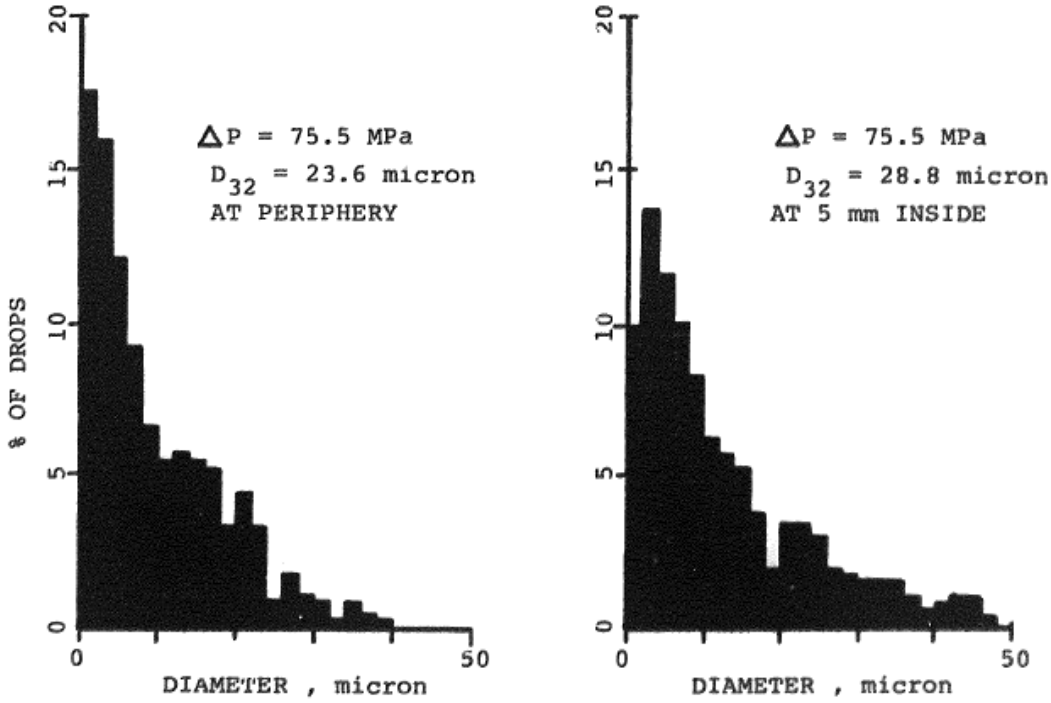

Figure 4.3. Influence of radial sampling location on PDF (Varde, 1984)

4.2.3 DNS as Validation Source

DNS offers the potential to study the physical processes of atomization outright by resolving all necessary time and length scales, and thus eliminating the need to model any unresolved scales. DNS makes an excellent analytical tool in the validation of primary breakup models. Being numerical in nature allows for the investigation into primary breakup in isolation of all secondary processes by merely deactivating specific components.

Fully-resolved DNS is not without its challenges however. Multiphase flows require additional length scale resolution the size of the smallest liquid structure, ζ. At the instant preceding droplet separation, the connecting ligament approaches zero, resulting in a length scale of zero. Thus, one must introduce a pinching model to address topology change. Obtaining grid independent solutions from the topology-change process is an issue of primary concern, and one that is often either under-resolved or overlooked in many recent

studies (see Herrmann 2008 for review). As a validation source, greater confidence may obviously be placed in DNS results that demonstrate some level of convergence.

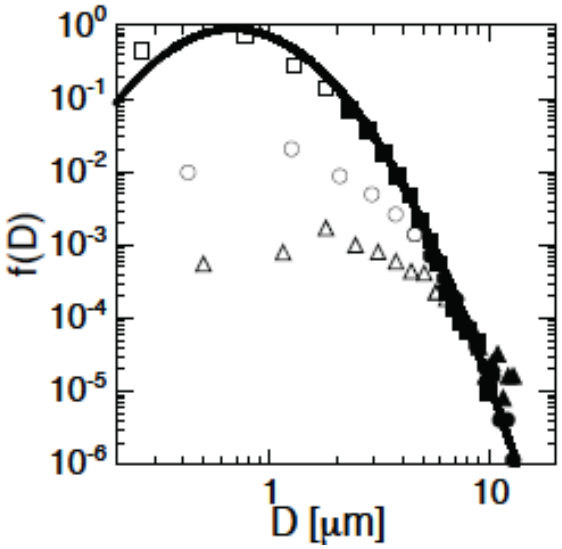

Figure 4.4. $f_N(d)$ convergence to Log-normal with spatial resolution (Herrmann, 2008)

The second difficulty of using DNS for model validation is the difference in operating regimes. To reduce computational cost, DNS tends to be conducted at significantly lower Reynolds and Weber numbers than those found under typical "diesel-like conditions". So much that DNS may be operating in the second wind-induced regime while diesel is exclusively found in the atomization regime. A solution to allow comparison despite this restriction is discussed further in Section 4.5.2.3.

4.3 Numerical Convergence

The governing equations of the ESE presented in Chapter 3 have derivatives in wavenumber space and time. Numerical simulation of the discretized ESE model thus requires consideration of grid resolution and convergence, as will be addressed in this

section. The parameter <N> was chosen as a measure of convergence because it concisely represents the entire drop-size histogram:

$$\langle N \rangle = \int_0^\infty f_N(d)\, dd$$

thus, convergence of <N> demonstrates a global convergence of the histogram. Convergence of the SMD was also demonstrated due to its popularity in characterizing atomizer performance.

4.3.1 Spatial Resolution

The derivative in k-space appears in the spectral energy transfer term in the ESE:

$$T_L(k) = -\frac{\partial \Pi}{\partial k} \quad .$$

The smallest turbulence length scales (large wavenumber) were resolved down to the Kolmogrov scale, η, with $k_{max} * \eta = \eta / \lambda_{min} = 2$. A logarithmic grid was employed to capture the energy present in the large turbulence scales up to the integral length scale, Λ, such that the minimum wavenumber is $k_{min} = 1/\Lambda$.

Then, progressively refining the grid spacing with fixed limits (k_{min}, k_{max}], <N> and d_{32} are shown in Figure 4.5 to converge with number of grid points. In this study the number of grid points in k-space were successively doubled, which effectively doubles the number of drop-size sampling 'bins'. A 5.4% increase in SMD can be seen during the first grid refinement. This would seem to indicate that spatial resolution of the first grid may be inadequate, especially at the largest wavenumbers due to the logarithmic grid.

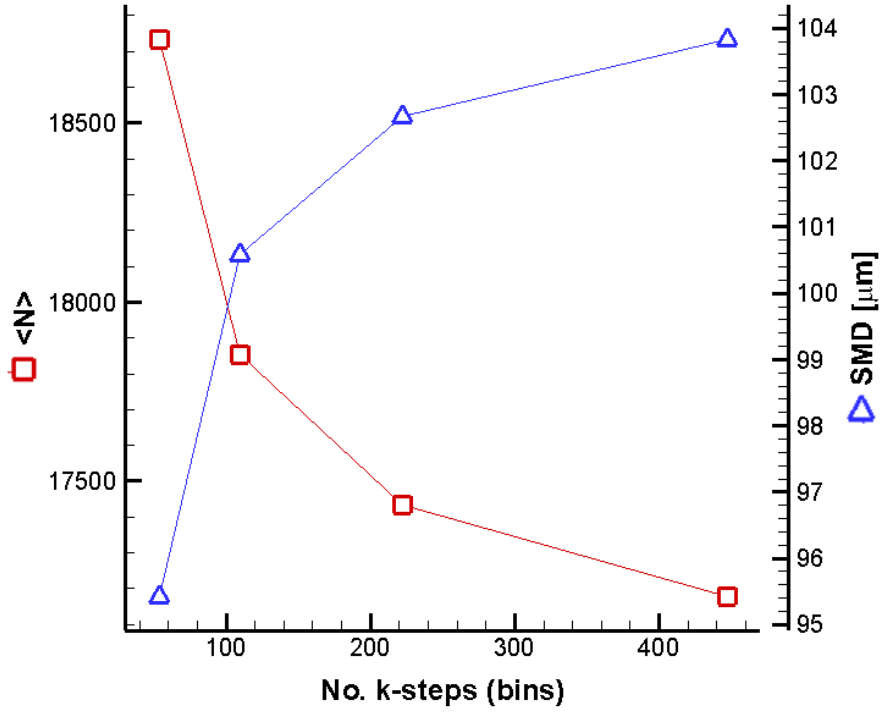

Figure 4.5. Convergence with spatial resolution

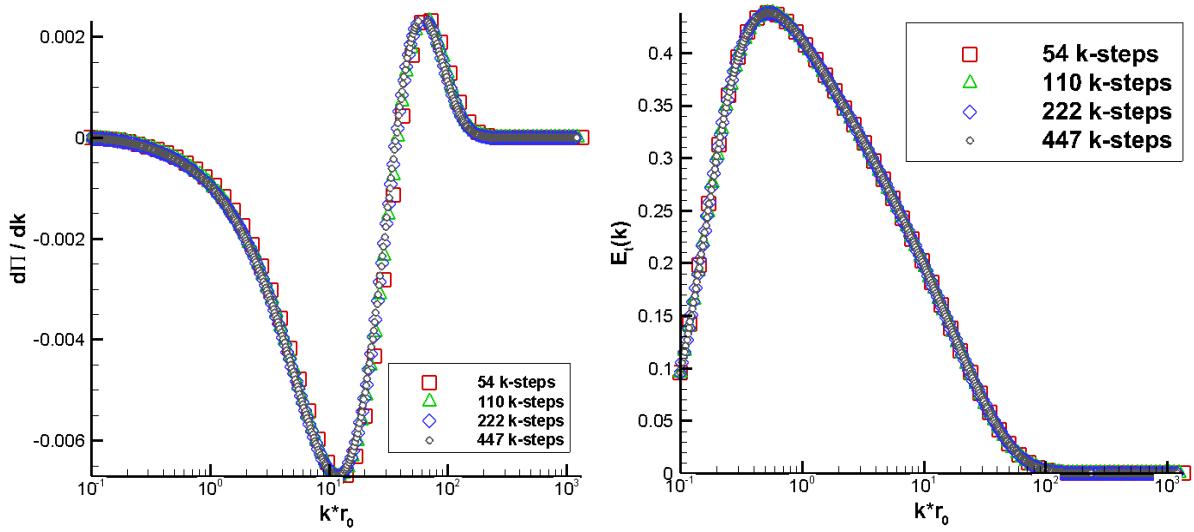

Figure 4.6. Convergence of $T_L(k)$ and $E_T(k)$ with spatial resolution

4.3.2 Temporal Resolution

The temporal derivative appears in the evolution equation when updating the energy spectrum. In all cases the simulation was run to a constant final time which was determined

to exceed the time to reach an approximate steady state solution. The normalized drop-size distribution was found to reach steady state at $(t/\tau_{\eta 0}) = 1500$, where, $\tau_{\eta 0}$ is the Kolmogrov time scale:

$$\tau_{\eta_0} = \left(\nu/\eta_0^2\right)^{-1} = \left(\frac{\nu}{(\nu^3/\varepsilon)^{1/2}}\right)^{-1} = \left(\frac{\nu}{\varepsilon}\right)^{1/2}$$

The first run time step size was set to 1/10 the duration of τ_η (i.e. $\tau_\eta/\Delta t = 10$), ensuring that all formation time scales are sufficiently resolved. Indeed, successive time step refinement yields only minor changes (0.7% difference) to the converging <N> and d_{32} measures, shown in Figure 4.5, implying that this default time step size is adequate for all cases used in this study.

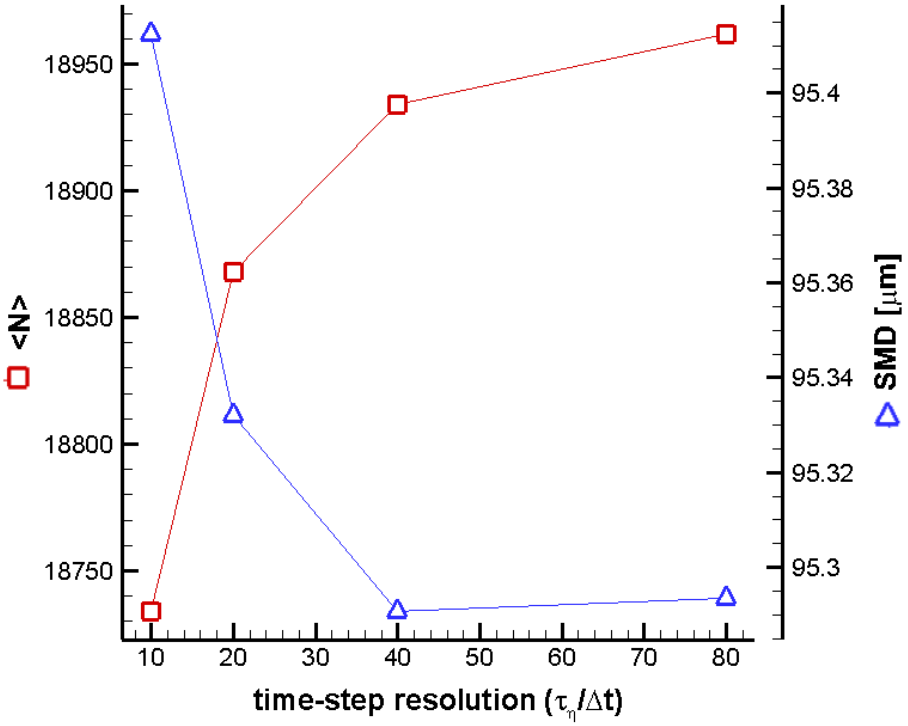

Figure 4.7. Convergence with temporal resolution

4.4 Sensitivity Analysis

In validating numerical simulations, it is important to investigate the model's sensitivity to model constants. Model constants are used to better represent physical phenomena. They are often 'tuned' such that the optimum value is the one that yields simulation results that are the best fit to the validation source's findings. However, equally important to the quality and confidence in a model is knowledge of how a given model constant will influence the outcome of the simulation, if varied.

Inspection of the governing equations reveals that the ESE model only utilizes 2 model constants: C_L and C_t. It is important to differentiate model constants from model parameters, such as Re_{T0}, We_L, and u'/U. Variation of model parameters is addressed in Chapters 4.5 and 4.6. For the purpose of the current sensitivity analysis, these parameters will be held constant, corresponding to typical diesel spray conditions, over all runs.

In the following subsections the purpose of each constant is described, default values and typical ranges are identified, and results of the sensitivity analysis are reported. The measure of sensitivity will be reported in terms of <N>, d_{10}, and $f_N(d)$.

4.4.1 Droplet Formation Constant, C_L

The drop formation constant, C_L, appears in the Wu and Faeth drop formation criterion to account for various geometric and scaling factors:

$$\rho_L V_L^2 \left(\frac{\pi\lambda^2}{12}\right) = C_L \left\{4\pi \left(\frac{\lambda}{2}\right)^2 \sigma\right\} .$$

C_L is approximated to be 1.52 by comparison with other work performed by the same authors. For the purposes of the sensitivity analysis, C_L was also set to 1 and 2. C_L is a very important parameter, having two influences.

First, it governs whether or not a drop could be formed at a given wavenumber. This is particularly important in the formation of small drop-sizes, where a large surface area to volume ratio requires massive amounts of kinetic energy to overcome the surface energy. Thus, the equations predict increasing C_L will increase the minimum dimensionless drop-size, d_{min}/d_0. The results of the sensitivity analysis reveal this trend to be correct; however, the difference is on such a small scale that overall impact is minimal. Inspection of Figure 4.8 reveals that the minimum drop-size decreased by $d/d_0 = 0.0011$ over the variation of C_L, which caused the mean drop-size to decrease by 0.8% overall.

Second, assuming enough energy exists at wavenumber, k, then this constant also influences the accumulation-formation threshold, E_d. Varying E_d in turn influences the frequency of formation given that the rate of energy accumulation is fixed by the drop formation time scale, τ_d. Thus, increasing C_L results in a uniform percent-decrease in f_N over all drop-sizes. Figure 4.8 demonstrates this phenomenon. Note that $f_N(d/d_0)$ and $<N>$ decrease proportionally, thus the normalized drop-size distribution, i.e. the PDF, is invariant.

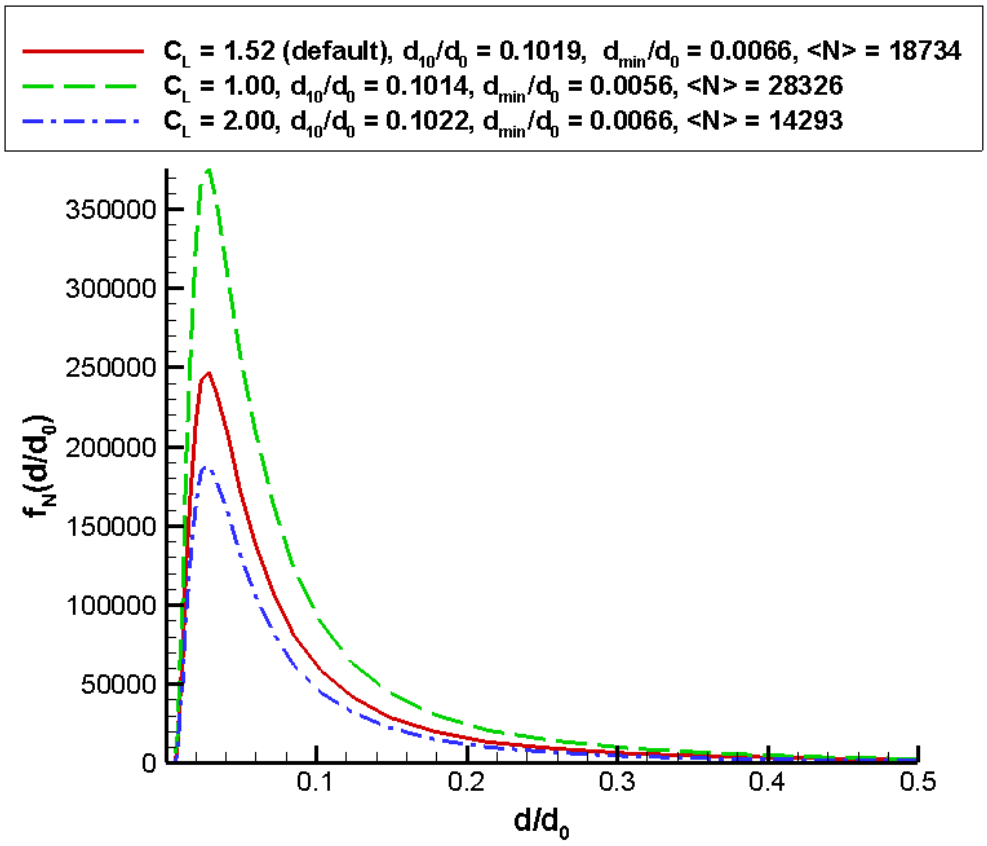

Figure 4.8. Results from C_L sensitivity analysis

4.4.2 Minimum Energy Threshold, C_t

This constant limits the energy drawn by the sink term such that the energy spectrum is always non-negative. In the event that the sink term attempts to draw energy that would result in the energy spectrum falling below C_t times the initial E_{11} at time t_{f0}, then an algorithm deactivates the sink term until enough energy has been restored. The optimum value of C_t must also be small enough so as to not have a large impact on droplet formation rate. The default value was chosen to be 0.3, with additional values of 0.2 and 0.4 selected for the sensitivity analysis.

The sensitivity analysis shows that the measures reported are invariant for the values of C_t chosen. The only explanation for this can be that the criterion preventing negative

energy spectrum was never triggered. In hindsight this makes sense as the Wu and Faeth formation criterion coupled with a relatively steady spectral energy transfer mechanism, ensures that the spectrum will remain well behaved under most 'diesel-like' conditions.

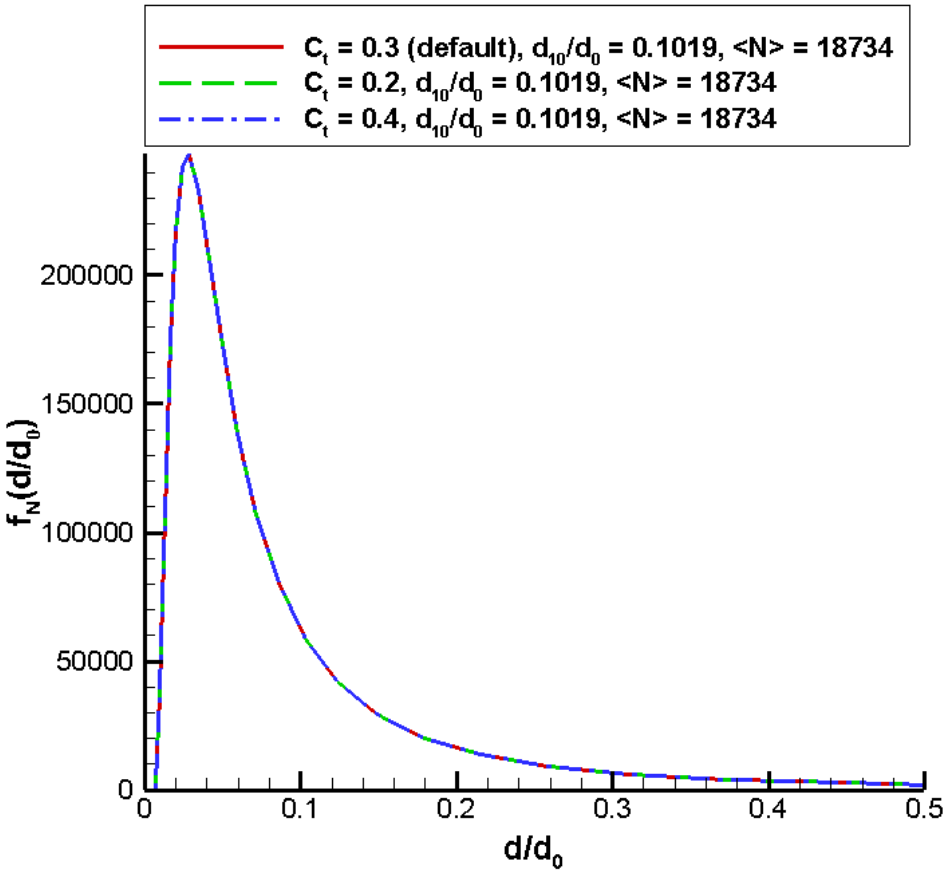

Figure 4.9. Results from C_t sensitivity analysis

4.5 Parametric Testing of Model: Influence of Injection Velocity on Histogram

4.5.1 Method

Three injection velocities, typical of diesel-like injection, were chosen corresponding to flow conditions reported in literature. The fluid properties were fixed over the three tests

to exclusively show the influence of velocity on the drop-size histogram. When necessary, reported dimensional fluid properties and flow conditions were converted to dimensionless Reynolds and Weber number for input into the ESE.

The first comparison source comes from the 1984 study conducted by Varde et. al. on high pressure plain orifice diesel injectors. The fluids used were No.2 diesel fuel injected into Nitrogen at standard temperature and pressure. Droplet sizes were obtained by exposing a sampling plate coated with a fluorochemical surface modifier to the 'mixing region' (see Figure 4.10) of the spray for a short duration. The droplets were analyzed electronically by a Quantimet 720, and subsequently drop-size distributions were constructed.

Comparison was conducted by analyzing the response of number-based PDFs. Varde gives $f_N(d)$ directly for the three injection pressures making comparison with ESE a straight-forward process.

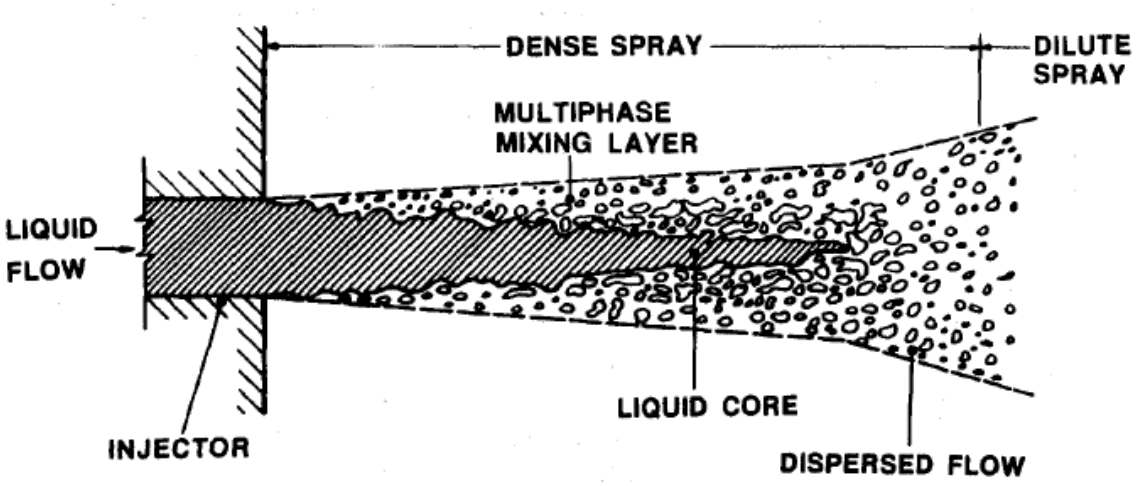

Figure 4.10. Schematic of near-injector region terminology (Faeth, 1995)

A second source for comparison was chosen to strengthen the analysis. The 1995 published results of Faeth et. al. were chosen as a second source for comparison due to its excellent applicability. Like the ESE model, Faeth's studies are relevant to turbulent primary breakup

of liquid jets ensuing from plain orifice nozzles into atmospheric gas. Faeth's experiments were primarily conducted on liquid water and glycerol jets with nozzle diameters one to two orders of magnitude larger than typical diesel nozzles; however, the dimensionless parameters, Re and We_L, are on par with those used in Varde's study and are indeed representative of modern diesel injection into atmospheric gas densities. Drop-size information was obtained in the 'dense spray' region by using double-pulse holocamera and reconstruction optics allowing accurate measurement of droplet diameters as small as 5 µm.

Contrary to the direct reporting of Varde, obtaining drop-size distributions from Faeth requires significantly more work. In their 1995 paper, Faeth et. al. gives the SMD correlation:

$$SMD = 0.65\, d_0 \left({}^{x}/_{d_0}\; We_L^{-1/2}\right)^{2/3} \quad ,$$

as a good fit to the experimental results for turbulent primary breakup in the dense liquid region. Furthermore, the authors note that all distributions were found to match the universal root-normal distribution given by Simmons (1977) with MMD/SMD = 1.2, where MMD is the mass median diameter. Given this information, it is thus possible to reconstruct the original PDF using only Faeth's SMD correlation, the cumulative number-based distribution function proposed by Simmons,

$$F_N(d) = 1.3882 \exp\left(-4.00 \left[{}^{d}/_{MMD}\right]\right) \quad ,$$

and the appropriate conversion to number-based PDF,

$$f_R = \frac{f_N(d)}{\langle N \rangle} = \frac{\left(\frac{dF_N(d)}{dd}\right)}{\langle N \rangle} \quad .$$

Simmons' distribution function was obtained by analyzing the CDFs of dozens of nozzles and noting that if the droplet diameters were normalized by their MMD, then all the curves would collapse down to a single distribution, thus demonstrating a 'self-similarity' among all injectors, as shown in Figure 4.11.

Since Faeth's results are given as a correlation shown to be valid over a large range of flow conditions, direct comparison with Varde and ESE is possible merely by computing the appropriate Weber number, dimensionless distance, and nozzle diameter.

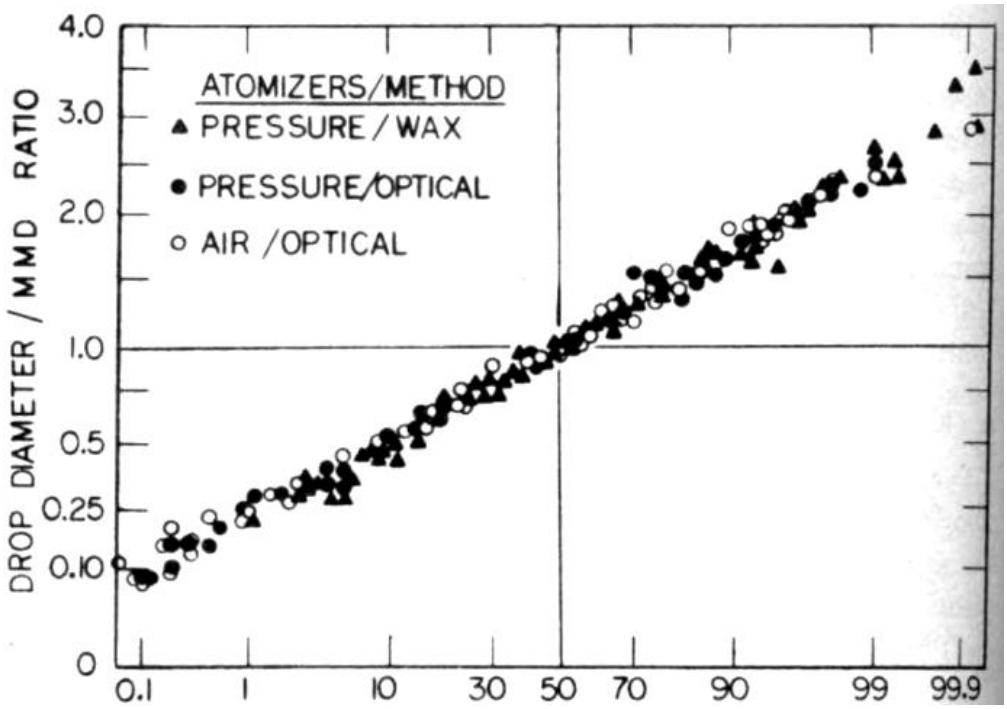

Figure 4.11. Simmons' normalization findings (Simmons, 1977)

4.5.2 Results and Discussion

The liquid injection velocity was varied between 327 and 421 m/s. The number-based PDF generated by the ESE model was compared with the experimental results of Varde (1984) and Faeth (1995), and with the Log-Normal and Chi-square distributions. The ESE model produces number-based PDFs that are in excellent agreement with published data

up to d = 60 μm (Figures 4.12 – 4.14), with the ESE model tending to slightly over predict the number of large droplets thereafter. Approximately 5% of all droplets formed by the ESE are larger than 60 μm. Thus, the large droplets' contribution to total error is small.

For the 3 injector velocities simulated, the PDFs generated by the ESE model matches well with the log-normal distribution. Reconstruction of Faeth's PDFs using Simmons' distribution revealed a tendency to form a large number of small diameter droplets akin to the Chi-square distribution, which differs from the ESE's prediction. As was noted in Section 4.5.1, the pulsed holography reconstruction method used in Faeth's experiments is unable to accurately measure droplets smaller than 5 μm. Thus, this discrepancy in the smallest drop-sizes could be due the continuous nature of Simmons' distribution, and may not necessarily be representative of the spray measured by Faeth. In the two lower velocity cases, Varde's PDFs demonstrate a reduced number of small droplets, similar to that of the Log-normal distribution and ESE. In the largest velocity case, Varde reports the results of two unique sampling locations. The default location, which he denotes 'at the periphery' closely matches the results of Faeth for the same flow conditions. The second, located 5 mm inside the periphery, best matches the ESE results, with more large diameter droplets formed at the expense of the small. As noted in Section 4.2.2, spatial sampling discrepancies can have a profound impact on the distribution.

Although somewhat cryptic, the word 'periphery' used by the author seems to be indicative of the boundary formed by the dense liquid region and the ambient gas, often referred to as the 'spray cone angle'. From this understanding, the secondary location, that is the one closer to the spray axis, would seem to be a better representation of primary breakup; since, as radial displacement from the liquid core increases, the influences of secondary

breakup and droplet coalescence are no longer negligible. Indeed, secondary breakup gives a plausible explanation for the large decrease in number of drops found between 30 and 50 μm and increase in number of drops found between 0 and 10 μm, as radial distance is increased. This would also indicate that the Log-normal distribution better represents pure primary breakup with respect to the smallest drop-sizes.

The ESE's response to variation of injection velocity, reflected in the number-based PDFs, is also noted to be in good agreement with the published results. The effect of increased jet velocity with fixed fluid properties is a decrease in mean droplet diameter, decreased variance, and an increased expected number of drops. The increased expected number of drops ascribed to the Wu and Faeth criterion, where increased kinetic energy results in the formation of more droplets over all wavenumbers. The reduction in mean and variance is attributed mostly to the variation of the total energy spectrum as a function of Reynolds number.

Finally, it is noted that a consequence of the over prediction of large diameter droplets is an increase in SMD. SMD has a (d^3/d^2) weighting and thus is highly sensitive to the formation of large droplets. The relevance of this last point will be seen in the second validation exercise.

In the following section, the formation of large droplets is considered further: two explanations are presented, followed by a discussion of their implications, and suggestions for future developments to improve the model.

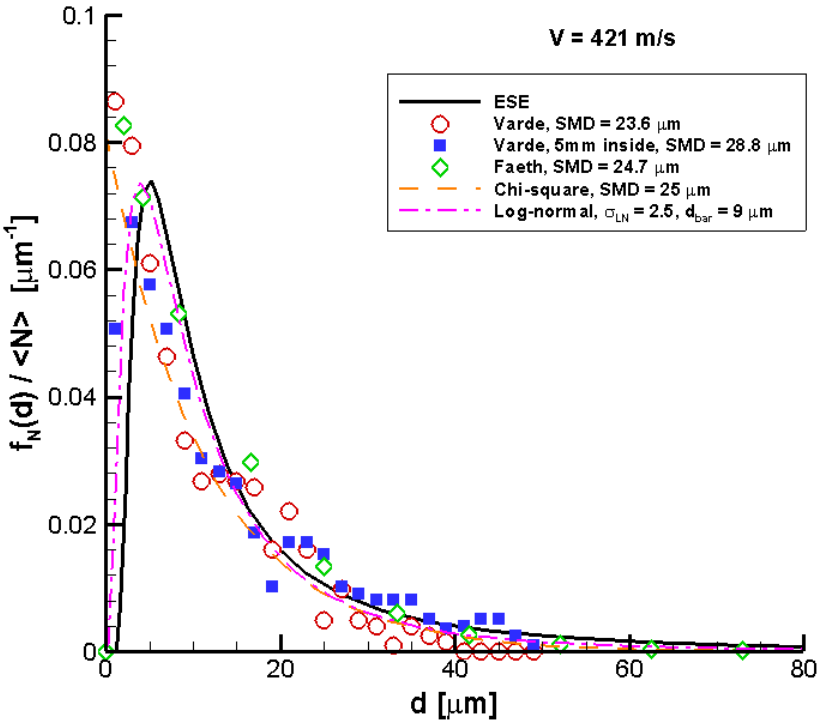

Figure 4.12. Drop-size PDF comparison, V = 421 m/s

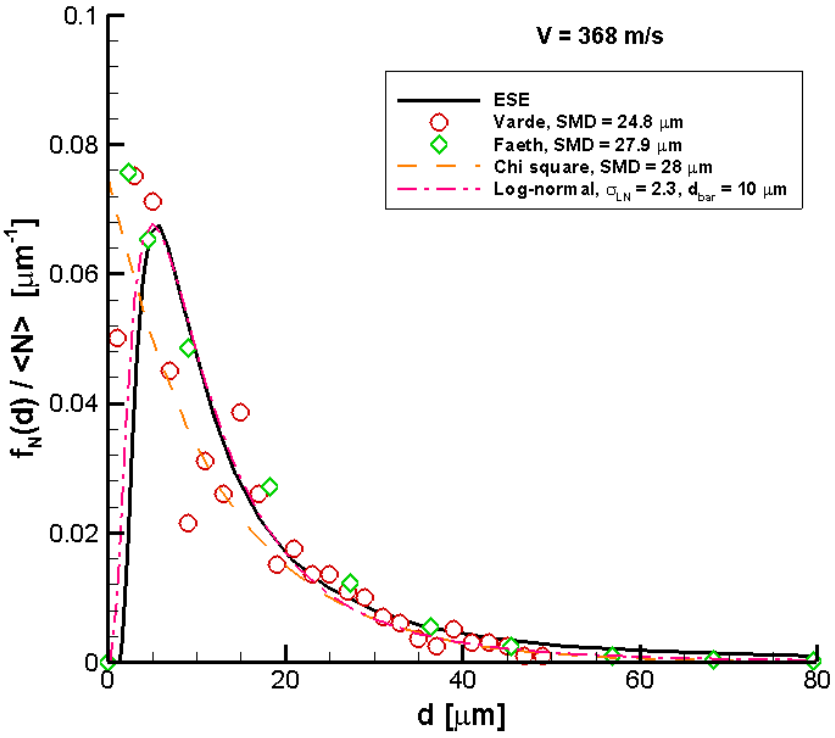

Figure 4.13. Drop-size PDF comparison, V = 368 m/s

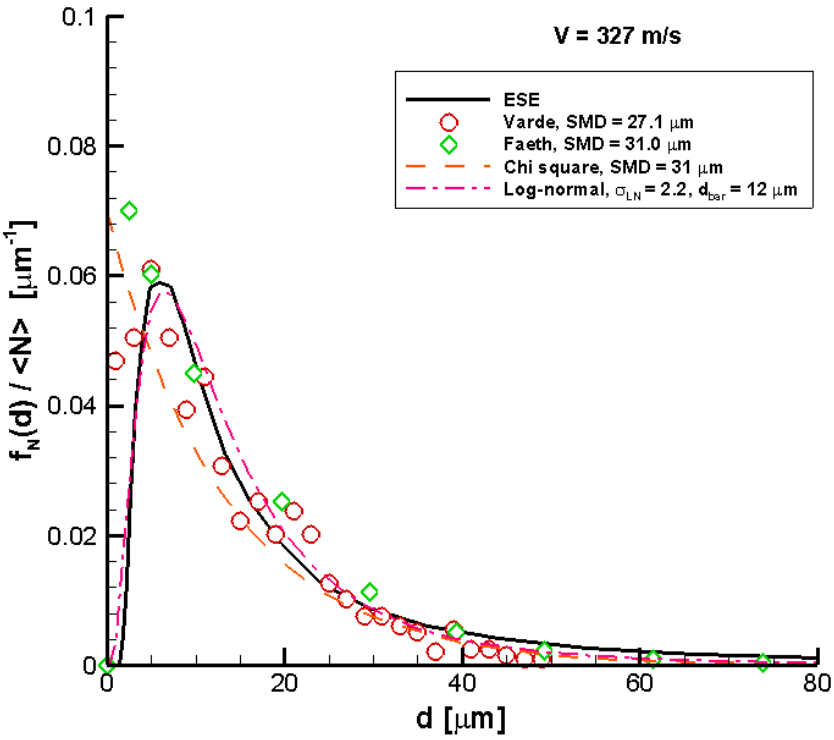

Figure 4.14. Drop-size PDF comparison, V = 327 m/s

4.5.2.1 First Hypothesis: Connection to secondary breakup

The first hypothesis attributes the over prediction of large diameter droplets in the ESE model to the breakup-type discrepancy between ESE and the validation sources; namely, that the ESE is strictly a primary breakup model, while experiments, and the correlations developed from them, can not entirely exclude the influences of secondary breakup, coalescence, etc.

The over prediction of large diameter droplets in the ESE model allows naturally for the future inclusion of a secondary atomization routine for further breakup. The 'blob' model was postulated to be an ideal candidate for such a coupling, as the two models display a sort of synergetic relationship. Each model addresses some of the shortcomings of the other, resulting in a more comprehensive unified model.

The blob model is inherently an aerodynamically driven secondary breakup model (see Section 2.2.1). As such, it is unable to properly capture the complete physics present in the liquid core. Indeed, this problem has been noted by several authors (Reitz, 1996; Reitz and Bracco, 1986; Chigier and Reitz, 1995) that although the 'blob' method is a reasonably complete model of low speed jets, it has difficulties with high speed jet breakup where initial turbulent nozzle flow becomes increasingly important. The ESE model in turn, is a turbulence driven primary breakup model, with the ability to model the effects of turbulent pipe flow; thus a coupling of models is postulated to resolve this problem.

The natural tie-in would be to use the ESE model to supply the initial droplet diameters into the blob model, thereby eliminating the initial mono-disperse 'blob' assumption. The ESE would supply a poly-disperse set of large diameter droplets for which the aerodynamic secondary mechanism would subsequently breakup, while also supplying a large number of small-diameter droplets formed as a direct consequence of the turbulence within the liquid core that may or may not undergo further breakup. Coupling in this manner should address the issue of dependence on nozzle flow in the blob model, while finding a natural way in which to resolve the formation of large droplets from the ESE.

Many drop-size filtering strategies exist to determine most probable drop-sizes to undergo secondary breakup. In this study, a lower limit constraint is defined for the smallest droplets formed by the ESE to undergo secondary breakup, d_{min2}. All droplets smaller than d_{min2} pass through the secondary model unscathed, however the PDF within this region will still be influenced by the addition of new, small droplets formed from the large. The cutoff value is obtained by the expression given by Lefebvre (1989):

$$d_{min2} = \frac{8\,\sigma}{C_D\,\rho_G\,U_R^2} \quad .$$

The figure below shows the influence of varying surface tension, σ, and relative velocity, U_R, typical of diesel sprays on the minimum droplet diameter for atmospheric gas densities. Note that in the present study, the cutoff diameter is approximately 10 μm; however, as gas density increases to 'diesel-like' conditions, the entire drop diameter range becomes susceptible to secondary breakup.

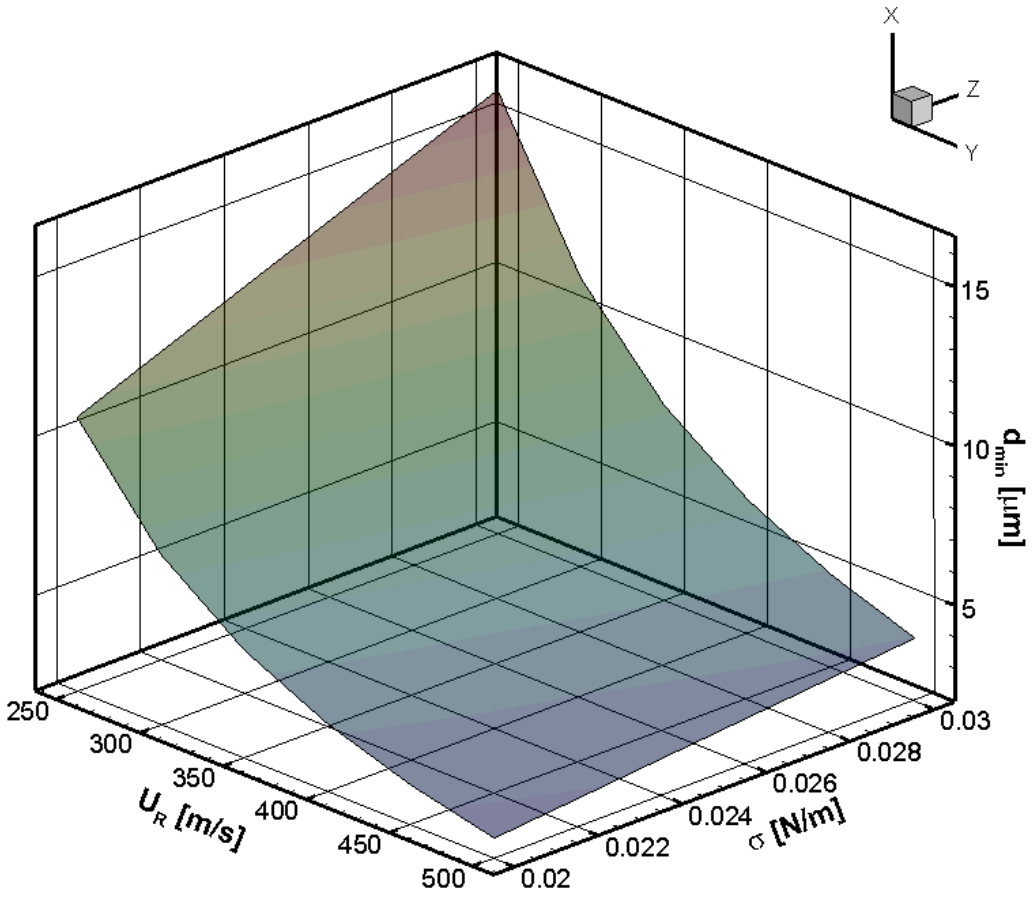

Figure 4.15. Lefebvre's correlation for d_{min}, constant ρ_G

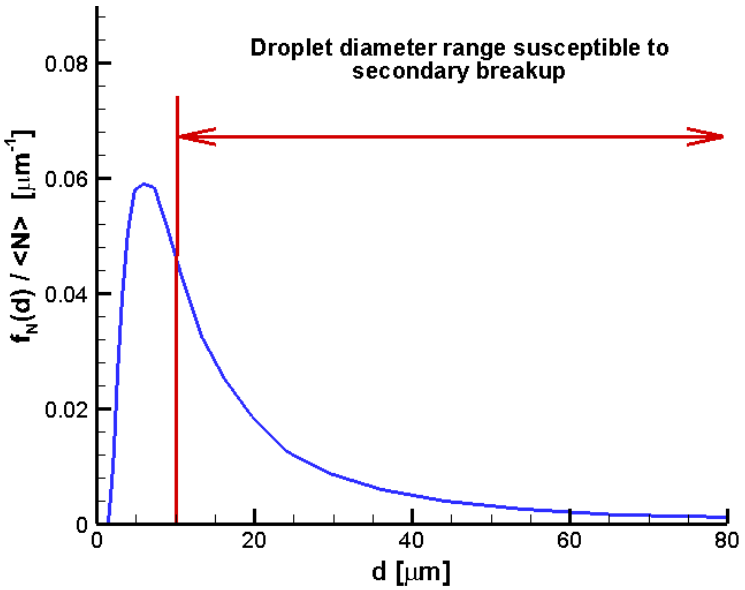

Figure 4.16. Lower drop-size limit susceptible to secondary breakup

4.5.2.2 Second Hypothesis: Energy Spectrum Representation

The second explanation for large droplets suggests that the current axisymmetric pipe flow energy spectrum may not be an appropriate model at the radial limits of the liquid core jet. The use of pipe flow energy spectra is an attractive assumption because it has been well-defined over the years (Niewstadt et. al. 1993, Lawn 1971) and is fairly representative of the plain-orifice nozzle geometry of diesel injectors.

The ESE model is capable of accepting any potential energy spectra obtained from DNS or experiments. The largest droplets originate from fluctuations approaching the order of the jet; thus, reductions in the number of large droplets could be realized if the new spectra were to contain lower energy densities in the wavenumber range ($1 \leq k\, d_0 \leq 5$). Published spectra from Niewstadt et. al. 1993 and Lawn 1971 both demonstrate that the spectra have some radial dependencies within this range (Figures 4.17 to 4.19); therefore, further investigation may be necessary in the future.

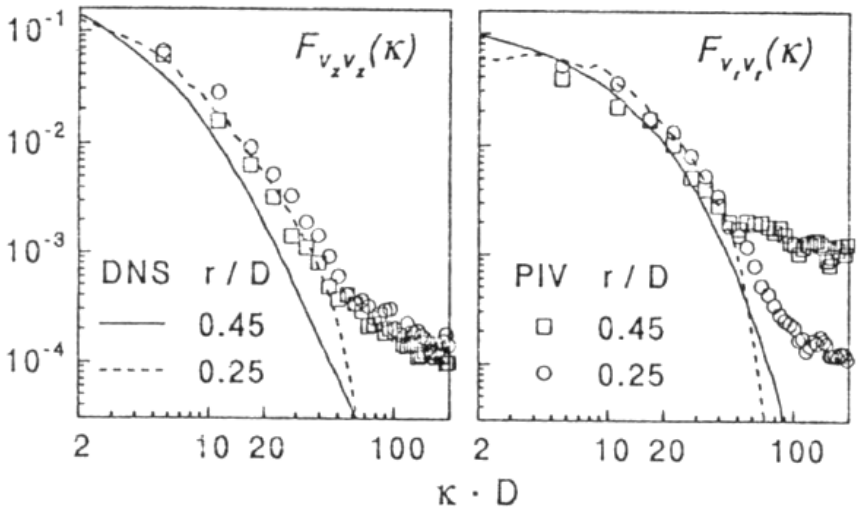

Figure 4.17. One-dimensional energy spectra of axial and radial velocity fluctuations, PIV = symbols, DNS = lines (Nieuwstadt, 1993)

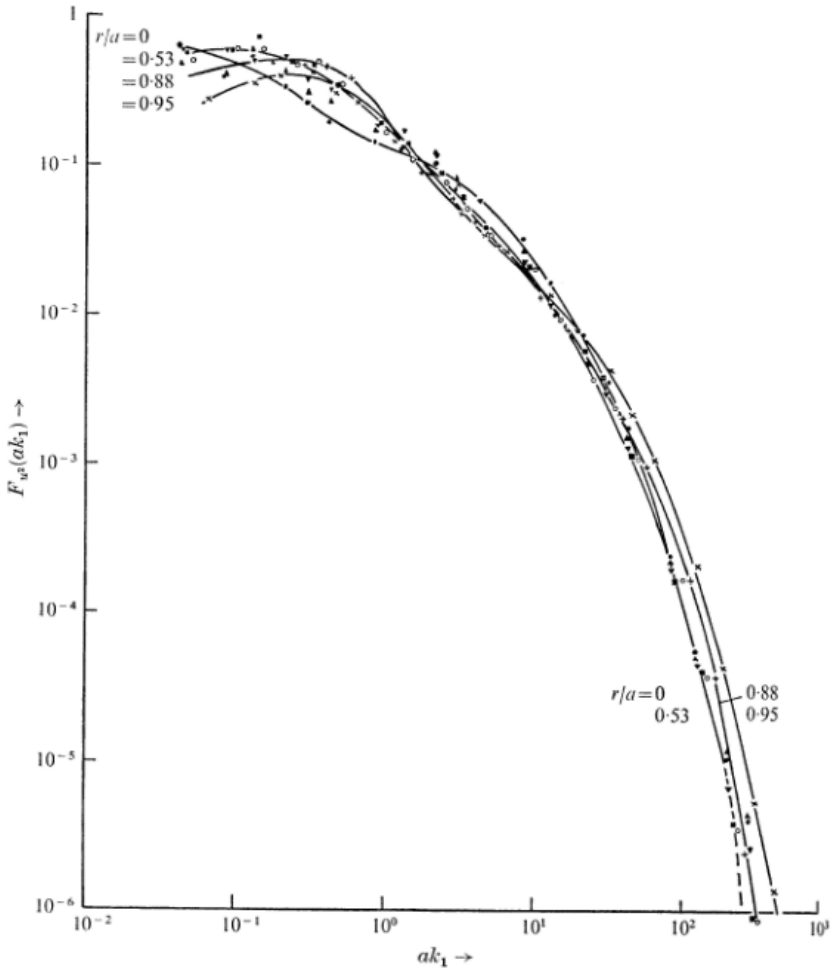

Figure 4.18. 1-D energy spectrum of axial velocity fluctuations (Lawn, 1971)

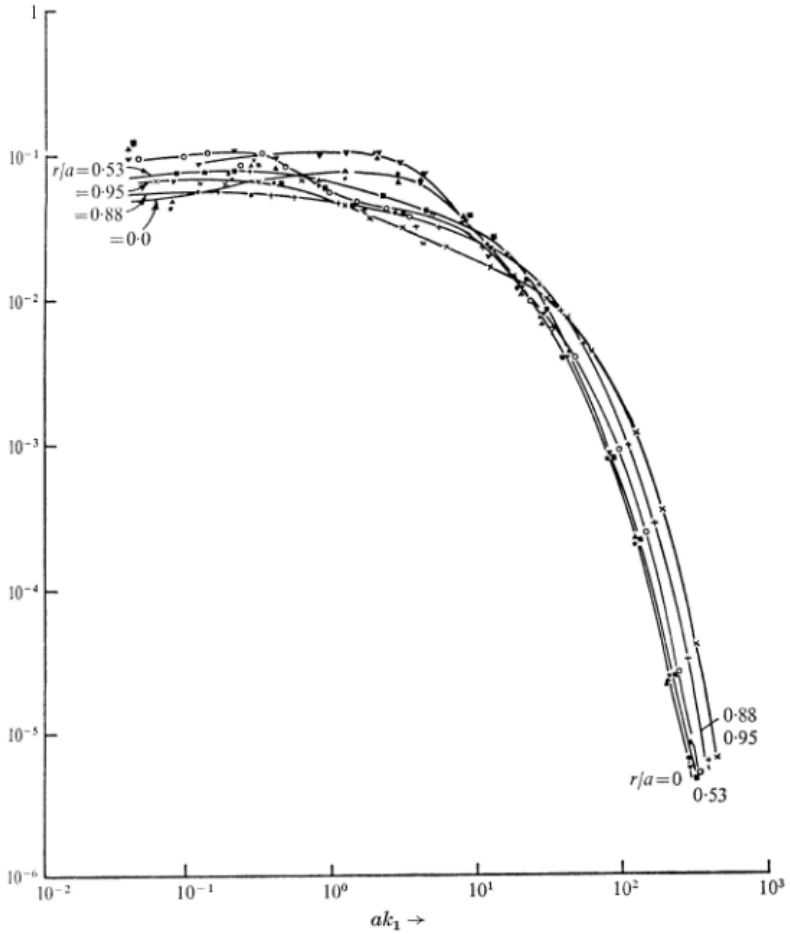

Figure 4.19. 1-D energy spectrum of radial velocity fluctuations (Lawn, 1971)

An alternative method was shown by Baumgarten et. al. (2002), in which the liquid core was discretized into two zones, each with their own energy spectrum, E_1 and E_2 (Figure 4.20). 'Zone 1' is characterized by a high liquid density region where turbulence effects dominate and an axisymmetric assumption is most valid. 'Zone 2' cannot be resolved purely by turbulence, thus cavitation effects are included here.

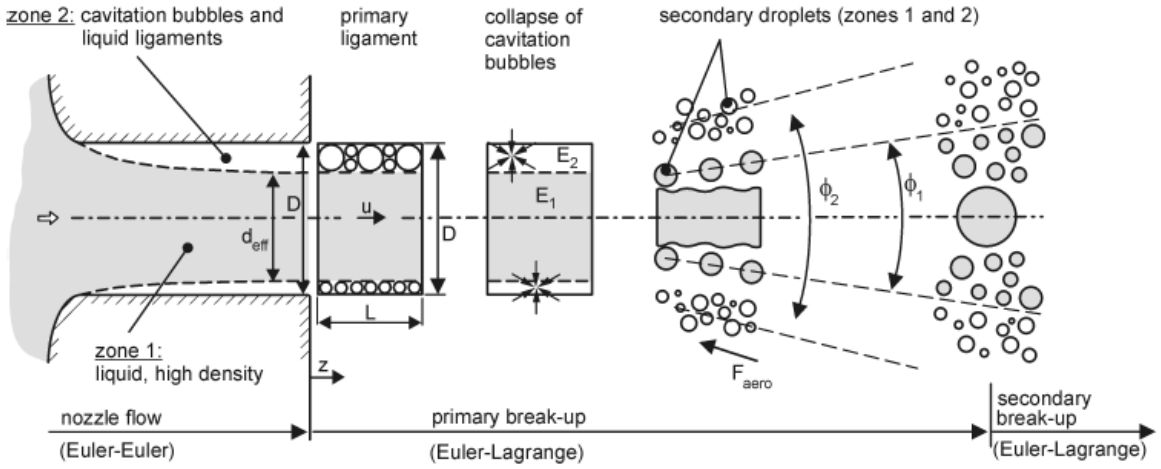

Figure 4.20. Two-zone Primary Breakup (Baumgarten, 2002)

4.5.2.3 Comparison with DNS

Comparison with DNS was performed to test the hypothesis put forth in Section 4.5.2.1, in an environment devoid of all secondary effects. The drop-size histogram of Herrmann (2008) was chosen for this comparison because it was obtained from pressure atomized sprays with secondary effects 'turned off' and solution convergence with grid resolution was demonstrated (see Figure 4.4).

It has been previously noted that interface-resolved DNS tends to be conducted at lower Re due to large computational cost. Indeed, with Re = 5000 and Oh = 0.026, Herrmann's study was clearly conducted within the 2nd wind induced regime (see Figure 4.1). This makes direct comparison under "diesel-like conditions" unfeasible with the current literature offerings. The problem may be bypassed if one were to normalize the PDF by the distribution's mean diameter, d_{10}. Parallel to the method of Simmons (1977), normalizing in this manner tends to collapse the distribution such that it may be expressed independently of the specific flow conditions. Distributions that exhibit this property are said to be 'self-similar'.

The results from this study are given in Figure 4.21. One immediately notes two things. First, the distribution of the small droplets (say, $0 < d/d_{10} < 4$) are similar, with both resembling the Log-normal distribution. This supports the previous findings that the Log-normal distribution is a better approximation for primary breakup than Chi-square. Second, one notes that the DNS distribution does not exhibit the large drop-size phenomenon found in the ESE. As a result, the scaled ESE distribution has a larger variance and the mode appears to be slightly left-shifted relative to the DNS distribution.

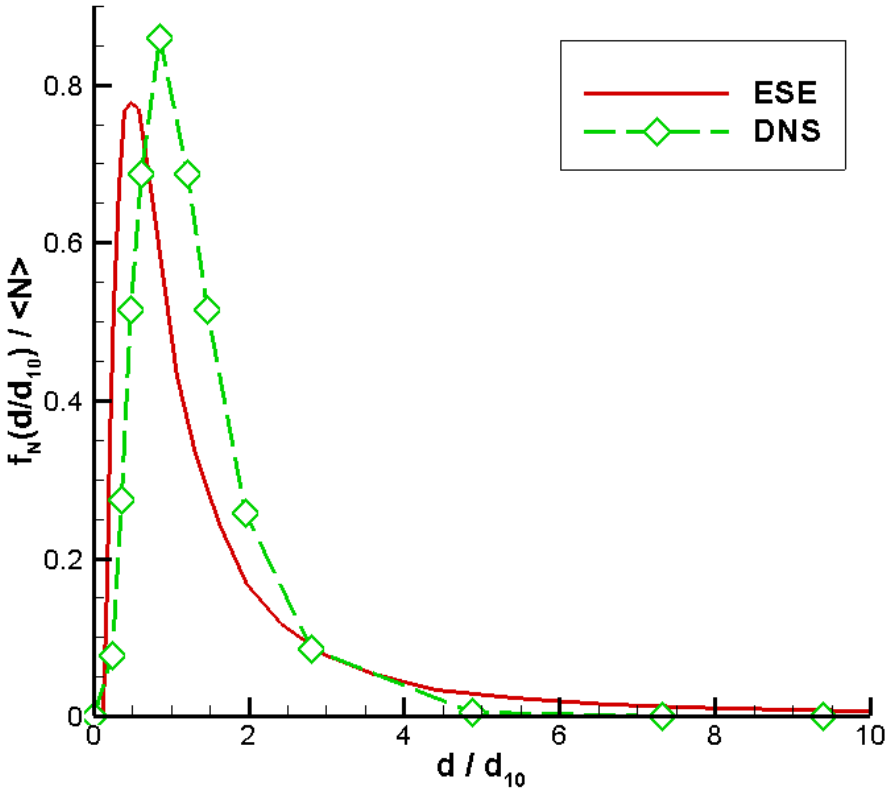

Figure 4.21. Comparison of ESE and DNS number-based PDF scaled by mean diameter

Fortunately, this discrepancy seems to be explainable on the basis of semantics. In the ESE, any detached liquid structure whose direct predecessor was the liquid core, is considered primary breakup. Herrmann's definition includes a constraint on the eccentricity

of the detached structure, such that only nearly-spherical droplets are reported in the primary breakup PDF. Detached liquid structures that do not satisfy this condition are allowed to undergo subsequent breakup until such time that the criteria has been satisfied for primary breakup. Using the semantics of the ESE model, such a process should be classified as secondary breakup.

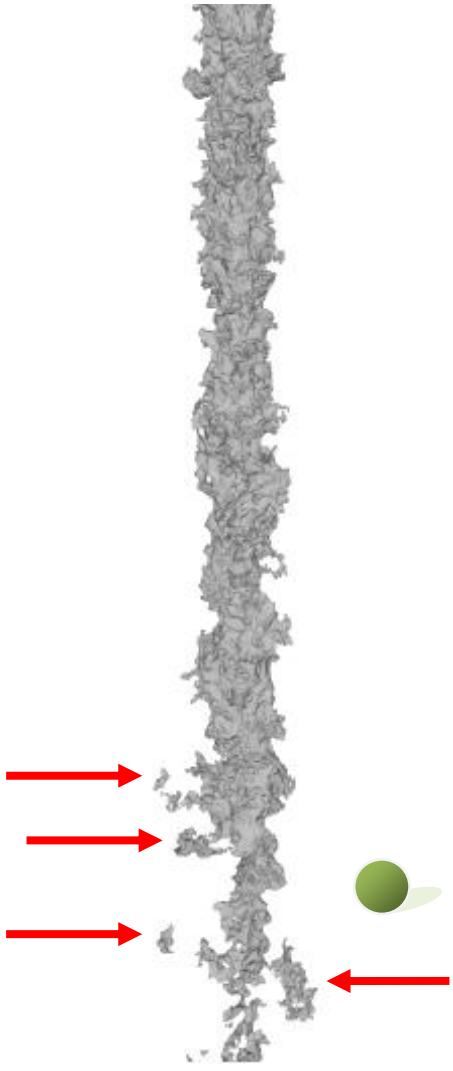

Figure 4.22. Liquid core structure from DNS (Herrmann, 2008), arrows indicate the presence of large detached liquid structures that do not meet Herrmann's criteria for primary breakup, green dot represents the maximum dimensionless drop-size predicted by the ESE

One clearly sees the consequences of this semantic discrepancy by viewing Figure 4.22. The arrows indicate the presence of a large detached liquid structure that would be reported by the ESE but do not meet the requirements of Herrmann. One also may note that the equivalent diameter of these detached structures approaches the maximum dimensionless drop-sizes predicted by the ESE ($d_{max}/d_0 < 0.73$) under 'diesel-like' conditions. The green dot in Figure 4.22 represents this maximum diameter prediction. The implications of this are profound, suggesting that the 'heavy-tailed' nature of the ESE's PDF may indeed be a correct representation for droplets arising solely from primary breakup.

4.5.3 Histogram Study Conclusions

Liquid injection velocity was varied between 327 and 421 m/s. The PDFs generated by the ESE model were compared with the experimental results of Varde (1984) and Faeth (1995), and with the Log-Normal and Chi-square distributions.

The ESE model produces number-based PDFs that are in excellent agreement with published data up to d = 60 μm, with the ESE model tending to slightly over predict the number of large droplets thereafter. Approximately 95% of the total area under PDF is less than or equal to 60 μm. ESE's response to variation of injection velocity is in good agreement with the published results.

The Log-normal distribution, which matches well with ESE, was concluded to better represent the formation of small drop-sizes under pure primary breakup conditions than the Chi-square distribution. The ESE's PDFs were normalized by d_{10} and compared with Herrmann's (2008) DNS results for primary breakup. Both distributions followed the Log-

normal distribution and evidence supporting the formation of large droplets was demonstrated.

Two hypotheses were presented. The first hypothesis attributed the over prediction of large diameter droplets in the ESE model to the breakup-type discrepancies between ESE and the validation sources which could not entirely be excluded. Furthermore, it was shown to provide a natural means for the future inclusion of a secondary atomization routine, such as the 'blob' model. Strategies were proposed to facilitate cohesion between primary and secondary models including a method for identifying droplets that will undergo secondary breakup. In the second hypothesis the appropriateness of the current energy spectrum representation at the radial limit of the liquid core was questioned. The two-zone strategy used by Baumgarten et. al. (2002) was noted as a possible solution.

4.6 Parametric testing of model: Influence of Liquid Properties on SMD

4.6.1 Method

For the second comparison test, parameters σ, ρ, and ν were varied in accordance with work performed by Ejim et. al. (2006) to simulate the effects of various biofuel blends on SMD. Such a predictive tool would be valuable in the investigation of new, potential alternative 'green' fuels.

Since the SMDs for ESE and validation sources differ due to the mechanisms discussed in the histogram parametric study, direct comparison is not possible. Rather, a demonstration that ESE exhibits the correct relative response to variations in fluid properties

is desired for validation test 2. Thus, 3 pure biofuels (B100) were selected in which to evaluate the percent-difference in SMD against No. 2 diesel fuel. The relevant fluid properties and corresponding dimensionless parameters are shown in Table 4.1. Additional parameters held constant include V_0 = 370 m/s, d_0 = 180 μm, ρ_G = 1.204 kg/m^3, and T = 273 K. The results from this analysis were then compared with several phenomenological correlations to judge ESE's sensitivity.

A large number of SMD correlations for pressure atomized sprays have been proposed over the years. An overview of the most popular and relevant correlations to turbulent primary breakup of high speed jets was presented in Chapter 2.1.1, including a detailed discussion of the ranges of applicability of each. The particular correlations chosen for this second validation test are Elkotb (1982), Varde (1984), Faeth turbulence and aerodynamically enhanced (1995).

Table 4.1 Fuel properties

Fuel type	ρ_L [kg/m^3]	σ [N/m]	ν [m^2/s]	Re	We_L
D2	801	0.02521	1.40E-6	47314	774511
Rapeseed	841	0.02782	2.58E-6	25674	736897
Soybean	841	0.02715	2.01E-6	32955	755082
Canola	841	0.02721	2.09E-6	31694	753417

First, a note on the ability of each the empirical correlation to properly represent varied fuel property is in order. This information will help us understand why a given

correlation reacted the way it did. The Elkotb correlation has a strong dependence on surface tension and liquid density, but a comparatively weak dependence on viscosity:

$$SMD_{Elkotb} = f\left(\sigma^{0.737},\ \rho_L^{0.737}, \nu^{0.385}\right) \quad .$$

The Varde correlation equally weights dependencies on surface tension, density, and viscosity, as represented by Reynolds and gas Weber numbers:

$$SMD_{Varde} = f\left(Re^{-0.28},\ We_G^{-0.28}\right) \quad .$$

The Faeth-turbulence correlation depends only on liquid Weber number, thus the influences of viscosity are neglected:

$$SMD_{Faeth\text{-}turb} = f\left(We_L^{0.333}\right) \quad .$$

As will be shown later, this deficiency makes the Faeth-turbulence correlation a poor choice for investigating alternative fuels. Finally, the improved Faeth-aero correlation depends strongly on density and viscosity, and weakly on surface tension:

$$SMD_{Faeth\text{-}aero} = f\left(\sigma^{1/6},\ \rho_L^{-5/12}, \nu^{1/2}\right) \quad .$$

4.6.2 Density Results

Results from the analysis revealed that the ESE model correctly predicts the general SMD trends (increase or decrease) in response to the various fluid properties (Figures 4.23 to 4.25). More specifically, the figures show that the ESE model possesses sensitivity to variations in liquid density that is in agreement with the Elkotb, Varde and Faeth-aero correlations. In the ESE model, the influences of liquid density are represented by the Reynolds and liquid Weber number which govern numerous aspect of the model, including the drop formation criterion given by Wu and Faeth:

$$\rho_L V_L^2 \left(\frac{\pi\lambda^2}{12}\right) = C_L \left\{4\pi \left(\frac{\lambda}{2}\right)^2 \sigma\right\} \tag{4.3}$$

Additional ρ_L dependence is due in part to the d_{max} cropping strategy proposed in Section 4.5.2.3, which uses the liquid-gas density ratio to compute core length.

Some limited dependencies on μ and σ may also be inferred from these figures; however, drawing unambiguous conclusions becomes a bit convoluted. Therefore, a more methodical variation of fluid properties is introduced in the following section.

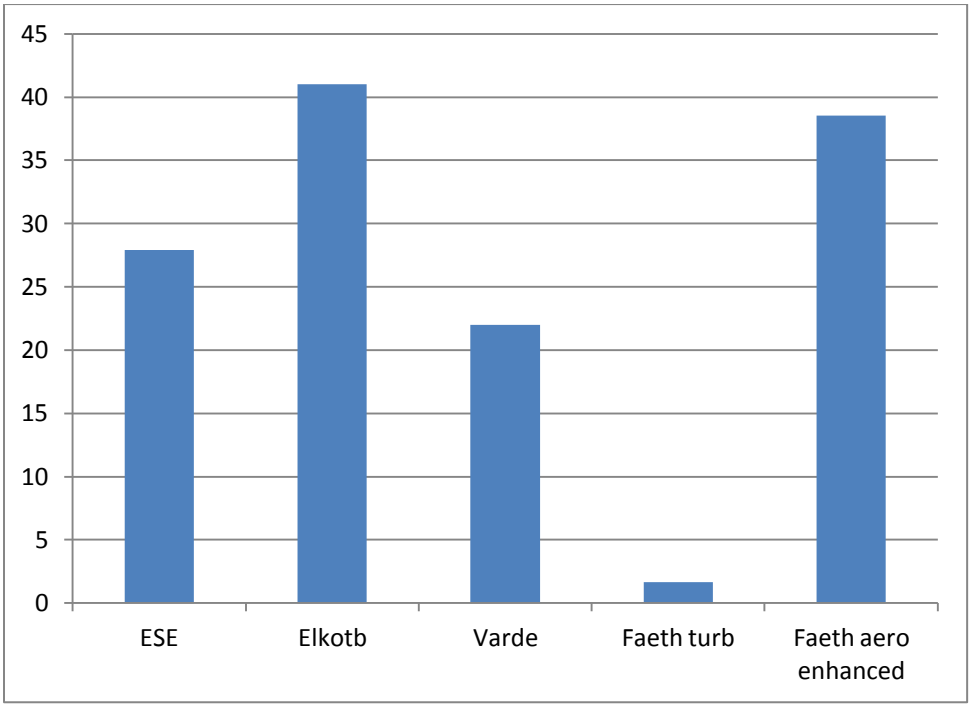

Figure 4.23. Effect of fuel property variation on SMD: Rapeseed versus D2, %-difference

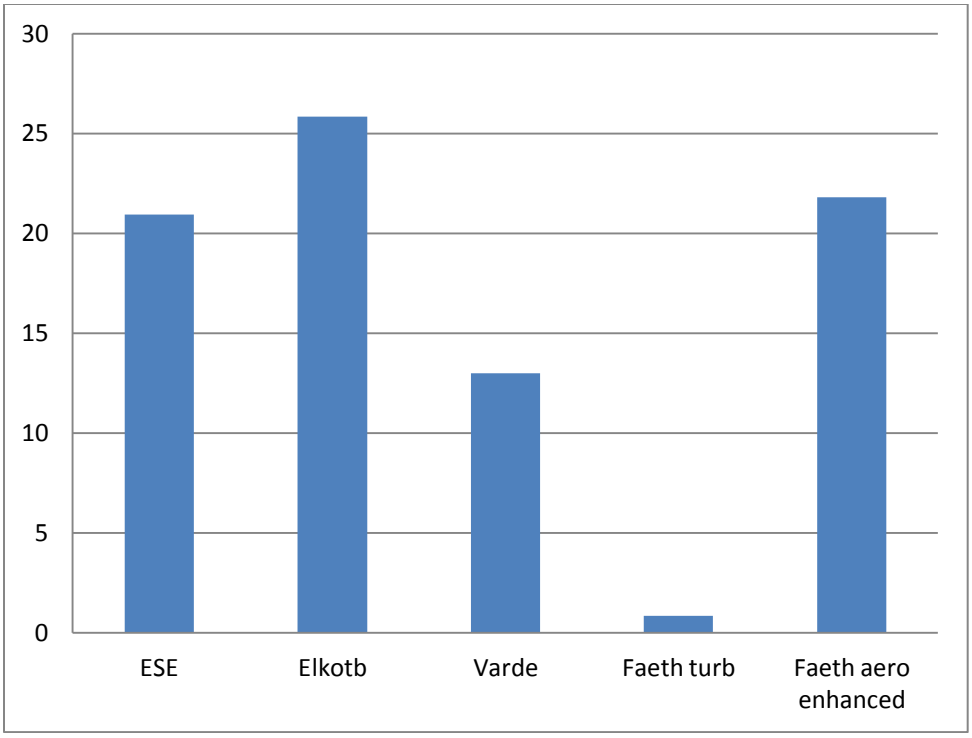

Figure 4.24. Effect of fuel property variation on SMD: Soybean versus D2, %-difference

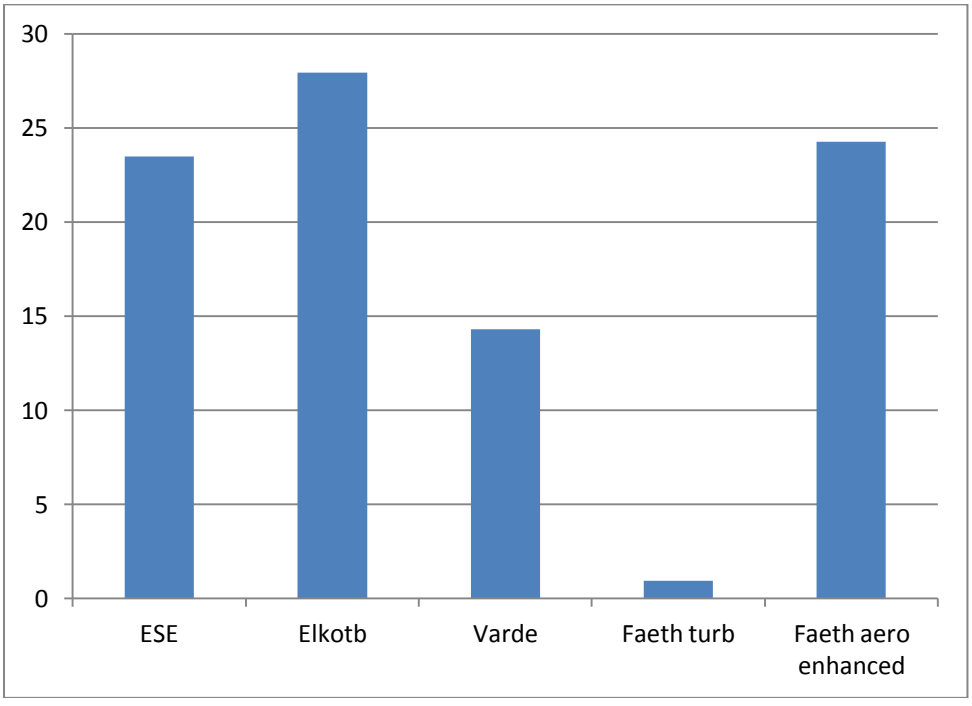

Figure 4.25. Effect of fuel property variation on SMD: Canola versus D2, %-difference

4.6.3 Viscosity and Surface Tension Results

The SMD's response to the systematic variation of dimensionless parameters Re and We_L was also investigated. Holding We_L constant and varying Re simulates a variation of viscosity, μ. Holding Re constant and varying We_L is analogous to the variation of surface tension, σ.

In the ESE, Reynolds number determines the pipe flow conditions, the initial energy spectrum, and turbulence timescales. The Weber number plays an important role in the surface energy term of Faeth's criterion, and also determines Rayleigh breakup timescales, when applicable. The dependencies of the empirical correlation have been introduced in the preceding section.

Figures 4.26 and 4.27 document the results of this investigation. Note that for direct comparison of slopes, two y-axis were used to account for the discrepancy in absolute SMD, but the scaling is equal. Figure 4.26 shows that the ESE is comparatively insensitive to variation of μ. This is interesting because Faeth's turbulence based correlation also demonstrates this insensitivity. All other correlations consider some aerodynamic effects (lower ρ_L/ρ_G), suggesting that some of the Re dependence of the ESE has been lost to additional breakup mechanisms. The response to varied σ predicted by the ESE is in excellent agreement with the Varde, Faeth turb, and Faeth aero correlations (Figure 4.27). Relative to the others, Elkotb's correlation seems overly sensitive to σ.

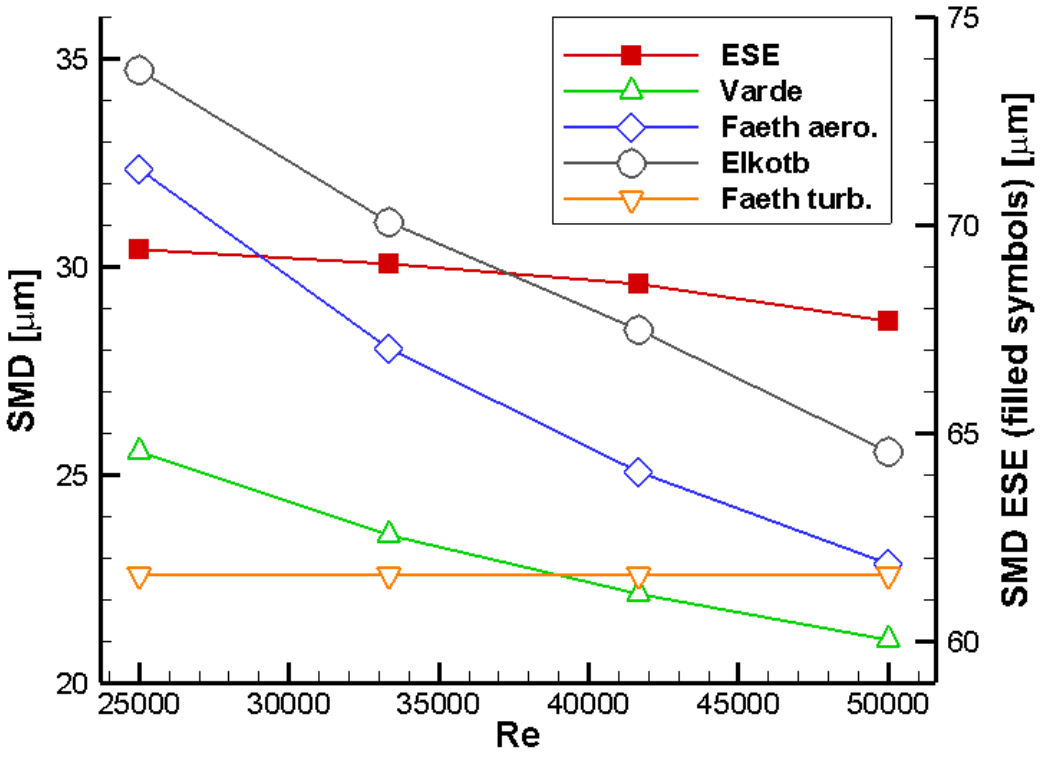

Figure 4.26. Effect of μ variation on SMD

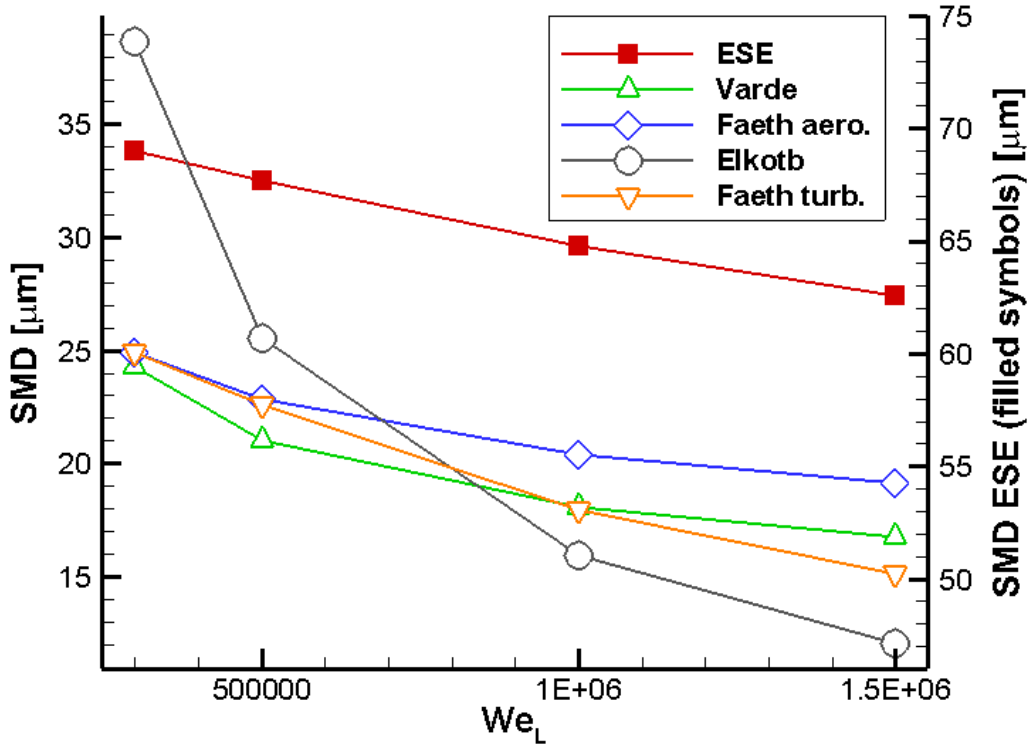

Figure 4.27. Effect of σ variation on SMD

CHAPTER 5. CONCLUDING REMARKS

The primary objective of this study was to investigate and validate a new spectral turbulence-based primary breakup model. In the first part of this study, the ESE model is described and successfully applied to diesel sprays to address the shortcomings of Lagrangian-type approaches to primary breakup.

In the second part of the study, the ESE was been shown to be numerically convergent with spatial and temporal resolution. Results of the sensitivity analysis show that the model constants are well behaved and that the solution is relatively insensitive to its variation.

Next, dimensionless parameters were varied in the ESE model to simulate different injection velocities over the typical range of injection velocities found under diesel-like conditions. In the drop-size range of interest for diesel sprays (0 – 80 μm), the ESE model was found to generate histograms which were in good agreement with experimentally obtained distributions found in literature and matched well with the Log-normal distribution. Also, a scaled PDF comparison with DNS for pure-primary breakup showed similar distributions of the small droplets.

A very small number of large diameter droplets ($d > 80$ μm) were also formed by the ESE in contrast to the validation sources' distributions; however, evidence supporting this finding was obtained from the DNS. Two plausible explanations were presented along with recommendation for future improvement. Connections to secondary breakup models and future integration into full-engine simulation codes were addressed. Of the secondary models reviewed, the 'blob' method was noted to be a good fit due to the complementary

nature of the two models. Also, connection to Baumgarten's two-zone approach was discussed, which naturally brings in influences of cavitation. This study originally set out to validate the ESE, an inherently turbulence-based primary breakup model; however, if one were to implement the recommendations proposed in this study into a future version of the model, then the ESE would essentially include all three principal breakup mechanisms.

In the second parametric study, dimensionless parameters were varied to simulate different fluid properties. The Sauter Mean Diameter generated by the ESE was compared to several popular phenomenological correlations. Although the absolute SMD magnitude differed between ESE and correlations, the ESE exhibited the correct response and sensitivity to variation of surface tension and density. Sensitivity of viscosity was found to be less that most correlations; however, greater that Faeth's turbulence-based correlation, suggesting that additional sensitivity may arise from the aerodynamic and cavitation breakup mechanisms.

BIBLIOGRAPHY

Amsdan A.A., O'Rourke P.J., Butler T.D., (1989) KIVA II: A computer program for chemically reactive flows with sprays. Los Alamos National Lab, LA-11560-MS

Arcoumanis, C., Gavaises, M., French, B., (1997) Effect of fuel injection process on the structure of diesel sprays. SAE Paper 970799

Baumgarten, C., Stegemann, J., and Merker, G. P. (2002) A new model for cavitation induced primary break-up of diesel sprays. ILASS-Europe

Blaisot, J.B. and Yon, J. (2005). Droplet size and morphology characterization for dense sprays by image processing: Application to the diesel spray. Experiments in Fluids, Vol. 39, pp. 977–994

Blaisot, J.B., Yon, J., (2005) Droplet size and morphology characterization for dense sprays by image processing: application to the diesel spray. Experiments in Fluids, Vol 39, pp. 977-994

Ejim, C.E., Fleck, B.A., Amirfazli, A. (2007). Analytical study for atomization of biodiesels and their blends in a typical injector: Surface tension and viscosity effects, Fuel, 86, pp. 1534-1544

Elkotb, M.M. (1982). Fuel atomization for spray modeling. Prog. Energy Combust. Sci., Vol. 8, No. 1, pp. 61-91

Faeth, G.M., Hsiang, L.-P., Wu, P.-k. (1995). Structure and breakup properties of sprays. Int. J. Multiphase Flows, Vol. 21, pp. 99–127

Faeth, G.M., Wu, P.-K., and Tseng, L.-K. (1992). Primary breakup in gas/liquid mixing layers for turbulent liquids. Atomization and Sprays, Vol. 2, pp. 295-317

Hermann, M. and Gorokhovski, M. (2008) Modeling primary atomization. Annu. Rev. Fluid Mech. Vol. 40, pp. 343-366

Herrmann, M. (2008) On simulating primary atomization using the refined level set grid method, ILASS 21st Annual Conference

Hiroyasu, H. and Katoda, T. (1974). Fuel droplet size distribution in diesel combustion chamber, SAE Trans., paper 74015

Huh, K.Y., Gosman, A.D., (1991) A phenomenological model of diesel spray atomization. Proceedings of International Conference on Multiphase flow.

Lawn, C.J., (1971) The determination of the rate of dissipation in turbulent pipe flow. J. Fluid Mechanics, Vol. 48(3), pp. 477-505

Lefebvre, A.H. (1989). Atomization and Sprays. Taylor & Francis.

Martinelli, L., Bracco, F.V., Reitz, R.D. (1984). Comparison of computed and measured dense spray jets. Progress in Astronautics and Aeronautics, Vol. 95, pp. 484-512

Nishimura, A., Assanis, D.N., 2000. A model for primary diesel fuel atomization based on cavitation bubble collapse energy. 8th International Conference on Liquid Atomization and Spray Systems, 1249-1256

Nieuwstadt, F.T.M., Westerweel, J., Eggels, J.G.M., Adrian, R.J., (1993) Direct numerical simulation of turbulent pipe flow. Applied Scientific Research, Vol. 51, pp. 319-324

Pope, S. (2009) Turbulent Flows. Cambridge Press

Reitz, R.D., 1987. Modeling atomization process in high pressure vaporizing sprays Atomization and Spray Technology 3, 309-337.

Reitz, R.D., Bracco, F.V., Wu, K-J. (1985) Measurements of drop size at the spray edge near the nozzle in atomizing liquid jets, Phys. Fluids Vol. 29(4), pp. 941-951

Simmons, H.C. (1977). The correlation of drop-size distributions in fuel nozzle sprays. Journal of Engineering for Power, Vol. 99, pp. 309-319

Sojka, P.E. and Babinsky, E. (2002). Modeling drop size distributions. Progress in Energy and Combustion Science, Vol. 28, pp. 303-329

Som, S. and Aggarwal, S.K. (2010) Effects of primary breakup modeling on spray and combustion characteristics of compression ignition engines. Combustion and Flame, Vol. 157, pp. 1179–1193

Stiesch, G. (2004). Modeling engine spray and combustion processes. Springer.

Subramaniam, S. A spectral model for the primary breakup of round turbulent liquid jets

Varde, K.S., Popa, D.M., Varde, L.K. (1984). Spray angle and atomization in diesel sprays, SAE Tech., paper 841055

ACKNOWLEDGEMENTS

I would like to take this opportunity to express my thanks to those who helped me with various aspects of conducting research and writing this thesis. First and foremost, I would like to express my gratitude to my advisor Dr. Shankar Subramaniam for his guidance and patience throughout this project. I would also like to thank my family for their continued encouragement and love. Finally, I would like to thank my fellow labmates and my committee members, Dr. Meyer and Dr. Kim, for all their support.